ORIGINAL ARTICLE

Optimization of polishing path and material removal for uniform material removal in optical surface polishing

Xingtian Qu[1] · Qinglong Liu[1] · Hongyi Wang[1] · Haizhong Liu[1] · Jiming Liu[1] · Huichao Sun[1]

Abstract

Uniform material removal affects the profile accuracy and surface quality of the optical surface in polishing. In general, polishing path planning and material removal optimization are studied separately. In this paper, the research combining these two aspects is employed to better ensure material removal uniformity and polishing efficiency. Two common polishing paths are covered: the scanning path and the concentric circle path. The scanning path is divided into the inner area and edge area, and the concentric circle path is divided into the peripheral area and central area, respectively. Material removal caused by the polishing path is analyzed by the simulation of the material removal map. For the scanning path, the spacing range is defined according to the number of superimposed removal profiles on the cross-section of the path, and the optimal spacing value in each spacing range is determined by using the numerical method. Then, the feed velocity is optimized to control the material removal thickness in the inner area, eliminate the over-polishing in the edge area, and ensure the polishing efficiency. For the concentric circle path, in the peripheral area, the influence of the path curvature on the removal profile is eliminated by optimizing the inclination angle and feed velocity, so that the spacing law of the scanning path can be applied to the concentric circle path. Furthermore, the over-polishing in the central area is eliminated by optimizing the radius of the central path, inclination angle, and feed velocity. Simulations and experiments are conducted to verify the feasibility of the proposed method. The results show that the proposed method can effectively improve the material removal uniformity, control the material removal thickness, and ensure the polishing efficiency.

Keywords Polishing path · Uniform material removal · Material removal profile · Process parameters

1 Introduction

Optical elements play an important role in the optical performance of optical systems. As the last process of optical surface manufacturing, polishing directly determines the final precision and quality of the polished surface. However, the traditional manual polishing has low efficiency and poor quality, which greatly tests the experience and technology of workers. With the development of the numerical control system (CNC), the automation of polishing has gradually matured [1]. Nowadays, many advanced polishing technologies have been proposed, including chemical

mechanical polishing (CMP) [2, 3], magnetorheological polishing (MRF) [4, 5], fluid jet polishing (FJP) [6, 7], ion beam polishing (IBF) [8, 9], and bonnet polishing [10, 11]. Automated polishing is very satisfactory due to its advantages of greatly improving the polishing accuracy and efficiency and reducing manufacturing costs [12]. When the flexible tool is adopted for polishing along the path, the local material removal is complex and inconsistent throughout the workpiece surface. However, uniform material removal is of great importance for ensuring profile accuracy and improving surface quality in polishing [13].

The polishing path has an important influence on material removal uniformity and polishing efficiency. Common polishing paths include the spiral path [14, 15], scanning path [16, 23], and concentric circle path [21]. In recent years, many studies on polishing path planning focused on improving the uniformity and coverage of the polishing path on the curved surface. Han et al. [14] proposed a cyclic iteration correction and driving method to generate the spiral path with physically uniform coverage

---

Xingtian Qu, Qinglong Liu, and Hongyi Wang contributed equally to this work.

✉ Hongyi Wang
    wanghongyi@jlu.edu.cn

Extended author information available on the last page of the article.

on the free-form surface. Zhao et al. [15] proposed the revised Archimedes spiral polishing path to ensure the physical uniform coverage of the aspheric surface based on the modified tool-workpiece contact model and the pointwise searching algorithm. Zhang et al. [16] defined the concept of the polishing ribbon and proposed a new scanning path planning method that can realize the physical uniform overlap of polishing ribbons on the free-form surface. However, the above researches directly substitute the uniformity and coverage of the polishing path for the uniformity of material removal and ignore the actual impact of process parameters (polishing pressure, polishing posture, feed velocity, etc.) on material removal, which can not directly ensure uniform material removal.

In the past few years, many scholars were working on the study of material removal models in order to accurately reflect and control the material removal in polishing. Zhang et al. [17] proposed the material removal profile model which represents the material removal depth distribution along the direction orthogonal to the polishing path. According to their studies, the material removal profile is almost parabolic and depends on the tool–surface geometry and the process parameters. Tam et al. [18] concluded that the material removal profile will bias toward the path curvature center under the influence of path curvature. Moreover, when the circular path curvature center is in the contact area, the shape of the material removal profile is not approximately parabolic but related to the radius of the path, and its removal depth is obvious. Fan et al. [19] studies show that the influence of path curvature on material removal profile can be eliminated by optimizing polishing posture angles. Furthermore, Fan et al. [20] modeled the material removal in the transition area for the round corner of the polishing path.

According to the above research, the material removal profile can be used to optimize the process parameters. Tam et al. [21] proposed a uniform polishing strategy for concentric circle path on the aspheric surface by calculating the superposition of material removal profiles on the aspheric meridian, which is used to optimize the feed velocity to achieve the given removal thickness. Fan et al. [22] derived the global polished profile model by convoluting the local polished profile along the measuring line, and the model is used to optimize the feed velocity to minimize the surface form error in polishing. These studies only optimize the process parameters without considering the importance of polishing path geometry (path spacing, turning area, edge area, central area, etc). If the spacing is selected to be relatively small, the polishing efficiency will be reduced. Moreover, due to the complexity of the material removal profile of the central path, the over-polishing will occur in the central area of the concentric circle path. However, the over-polishing can not be ideally improved only

by optimizing process parameters but also need to obtain the ideal removal profile by optimizing the path radius. The path spacing has an important influence on the superposition of material removal profiles. Tam et al. [23] analyzed the influence of path spacing on the material removal uniformity for the scanning path. According to their research, as the path spacing decreases, the more adjacent removal profiles are superimposed, and the material removal uniformity majorly tends to be better. However, when the number of removal profiles overlapping each other is large, the removal depth will increase significantly. At this time, it is necessary to control the removal depth by optimizing the process parameters. In addition, the over-polishing will occur in the edge area of the scanning path due to the superposition of the material removal caused by the two orthogonal straight paths. However, the over-polishing cannot be eliminated only by optimizating the path spacing, and the process parameters also need to be optimized.

According to the above analysis, compared with polishing path planning or material removal optimization, the combination of these two aspects may better ensure material removal uniformity and polishing efficiency. In this paper, for the polishing of the flat surface and the curved surface with large curvature radius, the research combining polishing path planning and material removal optimization is worked on. Two common polishing paths are covered: the scanning path and the concentric circle path. The scanning path is divided into the inner area and edge area, and the concentric circle path is divided into the peripheral area and central area, respectively. In this study, the spacing range is defined according to the number of superimposed removal profiles, and the path spacing and process parameters will be optimized according to the specific spacing range to improve the material removal uniformity, control the removal thickness and ensure the polishing efficiency.

In Section 2, the material removal map was calculated to analyze the global material removal. The optimization methods for the scanning path and concentric circle path were introduced in Section 3 and Section 4 respectively. Section 5 conducts the experiments to verify the feasibility of the proposed method in this paper. Section 6 summarizes the work of this paper.

2 3D material removal map

As shown in Fig. 1, the scanning path (SP) and the concentric circle path (CCP) are composed of straight paths and circular paths respectively. L represents the length of the straight path and R represents the radius of the circular path. The process parameters along every single straight path and circular path are constant in this paper. For SP and CCP, except in certain special cases, the local material

Fig. 1 (a) Scanning path and (b) concentric circular path
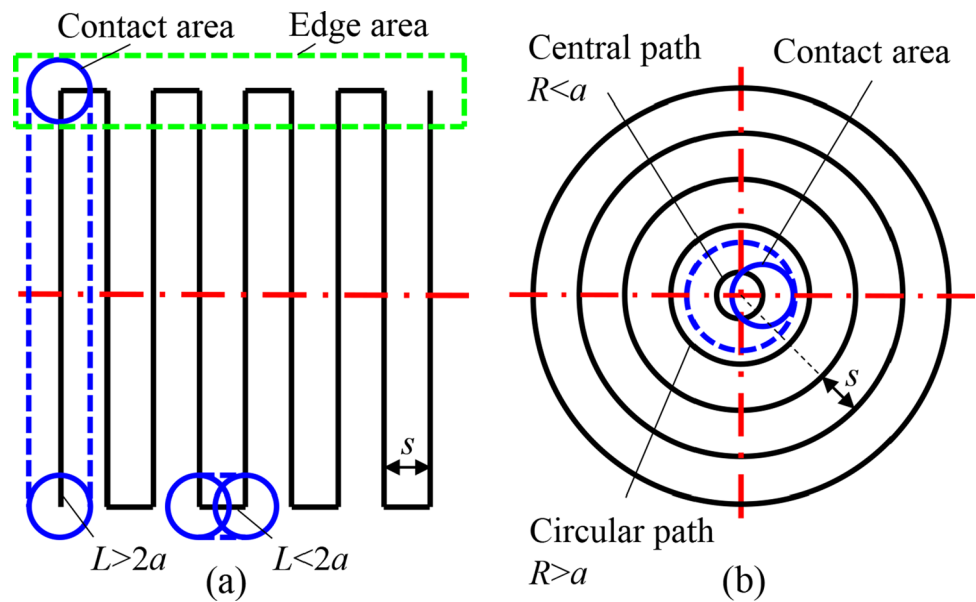
removal can be represented by the material removal profile proposed in the reference [19]. The material removal profile is obtained by integrating the material removal index along the polishing path in the contact area, which represents the material removal depth distribution along the direction perpendicular to the path. However, in some special cases, due to the integral form of the material removal index being different from that described in the reference [19], the local material removal cannot be represented by the material removal profile proposed in the reference [19]. For SP, the material removals in the contact areas at the start point and endpoint of the single straight path are the special cases. For CCP, the radius of the central circular path is usually smaller than the radius of the contact area, in which case the material removal caused by the central circular path is the special case. In this paper, the material removals in the above-mentioned special cases are modeled, and the 3D material removal maps [23] of SP and CCP are calculated to accurately reflect the global material removal.

2.1 Material removal profile model

Figure 2(a) and (b) are the schematic diagrams of the spherical tool polishing along the straight path and curved path at the feed velocity v_a, respectively. P is a polishing point on the polishing path. The Cartesian coordinate system $\{o; x, y, z\}$ is centered at point P and fixed to the part surface, such that the x-direction is perpendicular to the path, and the y-direction is tangent to the path. According to the Hertzian theory, a circular contact area will be formed between the spherical tool and the workpiece surface during polishing [24, 25]. H is a point on the x-axis in the contact area. When the tool passes through point H along the path,

L_1 and L_2 can be seen as the start point and endpoint for the contact area to pass through point H. Accordingly, $L_1 L_2$ can be regarded as the polishing ribbon of point H. The material removal depth at point H can be calculated by integrating the material removal index w_p along the polishing ribbon $L_1 L_2$, which can be expressed as [19]

$$h = \int_{L_2}^{L_1} w_p dl = \int_{L_2}^{L_1} K_p \frac{pv}{v_{ah}} dl \tag{1}$$

where K_p is the Preston coefficient, p is the contact pressure at point H, v is the sliding velocity at point H, and v_{ah} is the feed velocity of the tool across point H (In Fig. 2(a), $v_{ah}=v_a$; in Fig. 2(b), $v_{ah} = v_a \rho/R$, where R is the geodesic curvature radius of the curved path at point P).

Fan et al. [19] calculated the contact pressure distribution and sliding velocity distribution in the contact area, and further deduced the material removal profile considering the polishing posture by Eq. 1. If the contact area can completely across any point H on the x-axis in the contact area when the tool polishing along the straight path, the material removal profile for the straight path is given by [19]
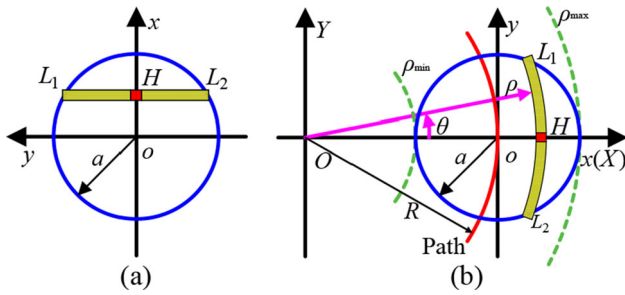
$$h(x) = -\frac{3K_p F_n \omega}{2\pi v_a a^3} \int_{-\sqrt{a^2-x^2}}^{\sqrt{a^2-x^2}} f(x, y)\, dy$$
$$-a \leq x \leq a \tag{2}$$

where

$$f(x, y) = \sqrt{ \begin{array}{c} (a^2 - x^2 - y^2) \\ \left[\begin{array}{c} (-R_p \sin\delta \sin\lambda - y\sin\delta)^2 \\ +(x\cos\delta + R_p \sin\delta \cos\lambda)^2 \end{array} \right] \end{array} } \tag{3}$$

where F_n is the normal polishing force, a is the radius of the contact area, ω is the rotational angular velocity of the tool, δ and λ are the inclination angle and declination angle

Fig. 2 Schematic of polishing along (a) a straight path and (b) a curved path

Fig. 3 Schematic of the straight path: (a) $L>2a$ and (b) $L<2a$

of the tool respectively defined in reference [19], and R_p is the distance from the tool center to the contact area.

When the curvature center O of the curved path is outside the contact area, the material removal profile for the curved path is given by [19]

$$h(\rho) = -\frac{3K_pF_n\omega R}{2\pi v_a a^3}\int_{-\arccos\left(\frac{\rho^2+R-a^2}{2R\rho}\right)}^{\arccos\left(\frac{\rho^2+R-a^2}{2R\rho}\right)} f(\rho,\theta)\,d\theta \qquad (4)$$

$$R-a \le \rho \le R+a$$

where

$$f(\rho,\theta) = \sqrt{\begin{bmatrix}(a^2-(\rho\cos\theta-R)^2-(\rho\sin\theta)^2)\\ \left[\begin{array}{l}(-R_p\sin\delta\sin\lambda-\rho\sin\theta\cos\delta)^2+\\ (\rho\cos\theta\cos\delta-R\cos\delta+R_p\sin\delta\cos\lambda)^2\end{array}\right]\end{bmatrix}} \qquad (5)$$

If a certain point H on the x-axis in the contact area is known, the material removal depth at point H can be calculated by Eq. 2 or 4.

2.2 Modeling of material removal in special cases

2.2.1 Special case of straight path

The straight path can be divided into $L>2a$ and $L<2a$ cases according to its length L, as shown in Fig. 3(a) and (b). I and E are the start point and endpoint of the straight path, respectively. The contact area at points I and E can be called the start point area and the endpoint area respectively. The process parameters along the straight path are constant. For the cases of $L>2a$ and $L<2a$, the polishing area of the straight path can be divided into three areas (α, β, and η) and four areas (φ, ϖ, ξ, and ψ) respectively. H is a point in the polishing area of the straight path. If point H is located in the area β or the area ϖ, the contact area can completely across point H when the tool polishing along the path. At this time, the material removal depth at point H can be calculated by Eq. 2. If point H is located in the start point area or the endpoint area of the straight path, the

contact area can only partially across point H when the tool polishing along the path. At this time, the polishing ribbon L_1L_2 needs to be determined specifically according to the polishing area where point H is located.

The frame XOY is fixed on the surface at points I and E, respectively, such that the Y-direction is tangent to the path and the X-direction is perpendicular to the path. The coordinates of point H in the frame XOY are (X, Y). According to Eq. 2, the material removal depth at point H can be expressed as

$$h(X,Y) = -\frac{3K_pF_n\omega}{2\pi v_a a^3}\int_{L_2}^{L_1} f(x,y)\,dy \qquad (6)$$

Next, the polishing ribbon L_1L_2 of point H located in different areas need to be determined according to the two cases of $L>2a$ and $L<2a$, and further calculate the material removal depth at point H by Eq. 6.

Case 1, $L>2a$

For the straight path in the inner area of SP, its length generally satisfies $L>2a$. In this case, the start point area and endpoint area of the straight path are denoted as α and η, respectively, which can be expressed in the frame XOY as

$$\left\{(X,Y) \mid X\in(-a,a)\,\&\,Y\in\left(-\sqrt{a^2-X^2}, \sqrt{a^2-X^2}\right)\right\} \qquad (7)$$

In the area α, the polishing ribbon L_1L_2 of point H is formed by the contact area moving from position 1 to position 2 (Fig. 4(a)). The coordinates of points L_1 and L_2 in the frame xoy are (X, Y) and $(X, -\sqrt{a^2-X^2})$, respectively, then the material removal depth at point H can be calculated as

$$h_\alpha(X,Y) = -\frac{3K_pF_n\omega}{2\pi v_a a^3}\int_{-\sqrt{a^2-X^2}}^{Y} f(X,y)\,dy \qquad (8)$$

In the area η, the polishing ribbon L_1L_2 of point H is formed by the contact area moving from position 3 to position 4 (Fig. 4(b)). The coordinates of points L_1 and L_2 in the frame xoy are $(X, \sqrt{a^2-X^2})$ and (X, Y), respectively, then the material removal depth at point H can be calculated as

$$h_\eta(X,Y) = -\frac{3K_pF_n\omega}{2\pi v_a a^3}\int_{Y}^{\sqrt{a^2-X^2}} f(X,y)\,dy \qquad (9)$$
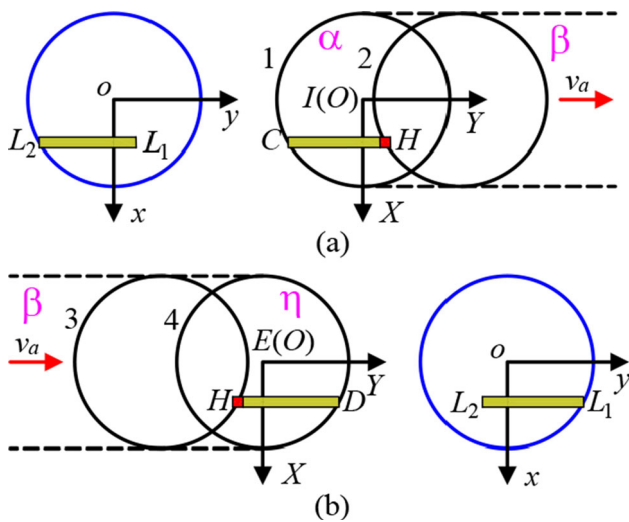
Fig. 4 The polishing ribbon L_1L_2 when $L > 2a$: (a) area α and (b) area η

Fig. 5 The polishing ribbon L_1L_2 when $L < 2a$: (a) area ξ and (b) area ψ

To sum up, for the case of $L > 2a$, the material removal depth distribution in the start point area and endpoint area of the straight path can be calculated as

$$\begin{cases} h(X, Y) = h_\alpha(X, Y), (X, Y) \in \alpha \\ h(X, Y) = h_\eta(X, Y), (X, Y) \in \eta \end{cases} \tag{10}$$

Case 2, $L < 2a$

For the straight path in the edge area of SP, its length usually satisfies $L < 2a$. In this case, the start point area and endpoint area of the straight path can be divided into three areas (φ, ξ, and ψ), which can be expressed in the frame XOY as

$$\begin{cases} \varphi = \left\{ (X, Y) \mid X^2 + Y^2 < a^2 \& Y < s - \sqrt{a^2 - X^2} \right\} \\ \xi = \left\{ (X, Y) \mid s - \sqrt{a^2 - X^2} \leq Y \leq \sqrt{a^2 - X^2} \right\} \\ \psi = \left\{ (X, Y) \mid X^2 + (Y - s)^2 < a^2 \& Y > \sqrt{a^2 - X^2} \right\} \end{cases} \tag{11}$$

According to Fig. 3(a), the modeling process of the material removal in the area φ is the same as that in the area α in the case of $L > 2a$, so there is $h_\varphi(X, Y) = h_\alpha(X, Y)$.

In the area ξ, the polishing ribbon L_1L_2 of point H is formed by the contact area moving from position 1 to position 2 (Fig. 5(a)). The coordinates of points L_1 and L_2 in the frame xoy are (X, Y) and $(X, Y - s)$, respectively, then the material removal depth at point H can be calculated as

$$h_\xi(X, Y) = -\frac{3K_pF_n\omega}{2\pi v_a a^3} \int_{Y-s}^{Y} f(X, y) \, dy \tag{12}$$

In the area ψ, the polishing ribbon L_1L_2 of point H is formed by the contact area moving from position 3 to position 2 (Fig. 5(b)). The coordinates of points L_1 and L_2 in the frame xoy are $(X, \sqrt{a^2 - X^2})$ and $(X, Y - s)$,
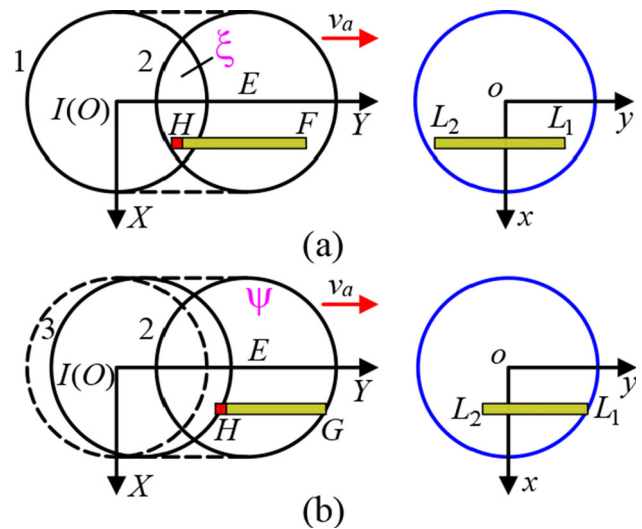
respectively, then the material removal depth at point H can be calculated as

$$h_\psi(X, Y) = -\frac{3K_pF_n\omega}{2\pi v_a a^3} \int_{Y-s}^{\sqrt{a^2 - X^2}} f(X, y) \, dy \tag{13}$$

To sum up, for the case of $L < 2a$, the material removal depth distribution in the start point area and endpoint area of the straight path can be expressed as

$$h(X, Y) = \begin{cases} h_\alpha(X, Y), (X, Y) \in \varphi \\ h_\xi(X, Y), (X, Y) \in \xi \\ h_\psi(X, Y), (X, Y) \in \psi \end{cases} \tag{14}$$

2.2.2 Special case of circular path

The circular path can be divided into $R > a$ and $R < a$ cases according to its radius R. The process parameters along the circular path are constant. For the case of $R > a$, the curvature center O of the circular path is outside the contact area (Fig. 2(b)), and the material removal caused by the circular path can be expressed by Eq. 4. For the case of $R < a$, the curvature center O of the circular path is within the contact area (Fig. 6), and the material removal caused by the circular path needs to be specially modeled. The polishing area of the circular path when $R < a$ can be divided into two areas, γ and ζ (Fig. 6). H is a certain point on the x-axis within these two areas. The calculation method of the material removal depth at point H is the same as that of Eq. 4, but the polishing ribbon L_1L_2 of point H needs to be specially calculated according to the areas γ and area ζ, respectively. The calculation process is as follows.

In the area γ, there is $\rho \in (0, a - R)$. As shown in Fig. 6, the polishing ribbon L_1L_2 of point H is a circle centered at point O and passing through point H. At this time, the upper
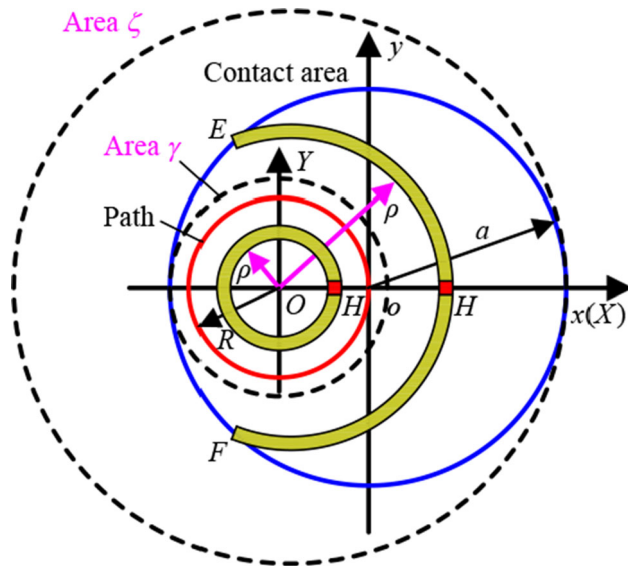
Fig. 6 The polishing ribbon $L_1 L_2$ when $R < a$

and lower limits of the integral of Eq. 4 are π and $-\pi$, then the material removal depth at point H can be calculated as

$$h_\gamma (\rho) = -\frac{3 K_p F_n \omega R}{2 \pi v_a a^3} \int_{-\pi}^{\pi} f(\rho, \theta) \, d\theta \qquad (15)$$

In the area ζ, there is $\rho \in (a - R, a + R)$. As shown in Fig. 6, the arc EF is the polishing ribbon $L_1 L_2$ of point H. At this time, the integral form is the same as that of Eq. 4. Therefore, the material removal depth at point H can be calculated by Eq. 4 as

$$h_\zeta = h(\rho) = -\frac{3 K_p F_n \omega R}{2 \pi v_a a^3} \int_{-\arccos\left(\frac{\rho^2 + R - a^2}{2 R \rho}\right)}^{\arccos\left(\frac{\rho^2 + R - a^2}{2 R \rho}\right)} f(\rho, \theta) \, d\theta$$

$$(16)$$

To sum up, for the case of $R < a$, the material removal depth distribution along the direction perpendicular to the circular path can be calculated as

$$h(\rho) = \begin{cases} h_\gamma(\rho), & 0 \le \rho \le a - R \\ h_\zeta(\rho), & a - R \le \rho \le a + R \end{cases} \qquad (17)$$

2.3 Simulations of the 3D material removal map

To predict the global material removal caused by SP and CCP respectively, the 3D material removal map [23] needs to be calculated respectively. Firstly, the polishing area of every single path is evenly divided into several discrete points to obtain the discrete point matrix. Then, the removal depth of each discrete point is calculated by the corresponding material removal model to obtain the removal depth matrix of the single path. Finally, all the removal depth matrices are superimposed and summed by MATLAB to obtain the global material removal depth matrix M_s. In

this paper, the depth of the 3D material removal map is taken as the positive value $(-M_s)$.

Next, the material removal caused by SP and CCP respectively is analyzed by simulations here. The spacing of SP is 1.8mm and the size of the polishing area is 20×20mm. For CCP, the radius of the central circular path is 0.9mm, the spacing is 1.8mm, and the polishing area is a circular area with a diameter of 20mm. In the simulations, the material of the flat workpiece is K9 glass. The parameters of the tool and the flat workpiece are listed in Table 1, and the process parameters are listed in Table 2. The simulation results are shown in Fig. 7(a) and (b). It can be seen that the 3D material removal maps of SP and CCP are light-dark alternating strip distribution and circular distribution respectively, which are the phenomenon of uneven material removal. In addition, significant over-polishing occurs in the edge area of SP and the central area of CCP. Considering the above points, this paper will next improve the uniformity of the global material removal caused by SP and CCP respectively by optimizing the polishing paths and material removal.

3 Analysis and optimization of the scanning path

SP is divided into the inner area and edge area here. The cross-section of the 3D material removal map is the 2D material removal profile [23]. When the curvature radius of the workpiece surface is much larger than that of the polishing tool and the surface curvature changes relatively small throughout the workpiece surface, the effect of the surface curvature on material removal variation can be ignored. The process parameters along every single straight path are constant. In this paper, the workpiece surface is directly selected as the flat surface. Since the surface curvature and path curvature are constant, the material removal profile is constant throughout the inner area. Therefore, the 2D material removal profile is sufficient to reflect the material removal in the inner area. In this section, the 2D material removal profile will be first calculated to reveal the material removal uniformity and material removal depth. Then the uniformity of the material removal in the inner area will be improved by optimizing the path spacing and process parameters. Lastly, the over-polishing in the

Table 1 Parameters of tool and workpiece

Parameters	Tool	Workpiece
Shape (mm)	Sphere: R_t=8	Cylinder: Φ=60
Material	Polyurethane	K9 glass
Young's modulus (Gpa)	E_t=0.01	E_w=88
Poisson's ratio	υ_t=0.3	υ_w=0.215

Table 2 Process parameters

Parameters	Values
Normal polishing force F_n (N)	5
Angular rotational velocity ω (rad/s)	125
Feed velocity v_a (mm/s)	0.02
Inclination angle δ (°)	30
Declination angle λ (°)	SP: 0, CCP: 90

edge area will be analyzed by using the 3D material removal map and eliminated by optimizing the process parameters.

3.1 2D material removal profile and related calculations

3.1.1 2D material removal profile and spacing range

As shown in Fig. 8(a), O is the center point of SP, the coordinate system $\{O; X, Y, Z\}$ is fixed on the surface at point O, and SP is located on plane XOY. In the inner area of SP, P_0 is the 0th straight path through the center point O, and P_i represents the ith straight path, where $i \in (-N, N)$. The total number of the straight paths in the inner area of SP is $2N+1$. The length and width of the rectangular polishing area are L_x and L_y, respectively. If the spacing of SP is s, N should satisfy the relationship $Ns < L_x/2 < Ns + s$. Moreover, the length of path P_i is L_y.

The section profile of the 3D material removal map (Fig. 8(b)) along plane XOZ is the 2D material removal profile (Fig. 8(d)). The depth of the 2D material removal profile is taken as the negative value. The 2D material removal profile can be obtained by overlapping the material removal profiles associated with the straight paths in the inner area, which can be expressed as

$$S(X, s, v_a) = \sum_{i=-N}^{N} h_i (X - is) \tag{18}$$

where $h_i(X)$ represents the ith material removal profile in the frame XOY.

The 2D material removal profile S can be seen as the function of the coordinate X, path spacing s, and feed velocity v_a.

The 2D material removal profile is wave due to the overlapping of the material removal profiles. Since both the material removal profile and the spacing s are constant, the fluctuation of the 2D removal profile is periodic, and the period is the spacing s. m is the number of material removal profiles superimposed on each other in a spacing period, which is related to the range of spacing s. The spacing range $s \in (2a/n, 2a/(n-1))$ is defined as the nth spacing range (n is an integer greater than 0) here. When $s \in (2a/n, 2a/(n-1))$, two secondary profiles [23] will be generated in an spacing period due to the overlappings of $n-1$ and n material removal profiles respectively, as shown in Fig. 9(a). When $s = 2a/n$, only one secondary profile [23] will be generated in a spacing period s due to the overlapping of n material removal profiles, as shown in Fig. 9(b).

### 3.1.2 Evaluation parameters for the material removal uniformity

According to Eq. 18, the removal depth caused by the superposition of m material removal profiles in a spacing period can be expressed as

$$H_m(X, s, v_a) = \sum_{i=0}^{m-1} h_i (X - is, v_a) \tag{19}$$

When m is odd, i.e., $m = 2k + 1$, substituting $X = ks$ into Eq. 19, the maximum removal depth of H_m can be calculated as

$$(H_m)_{\max}(ks, v_a) = \sum_{i=0}^{m-1} h(ks - is, v_a) \tag{20}$$

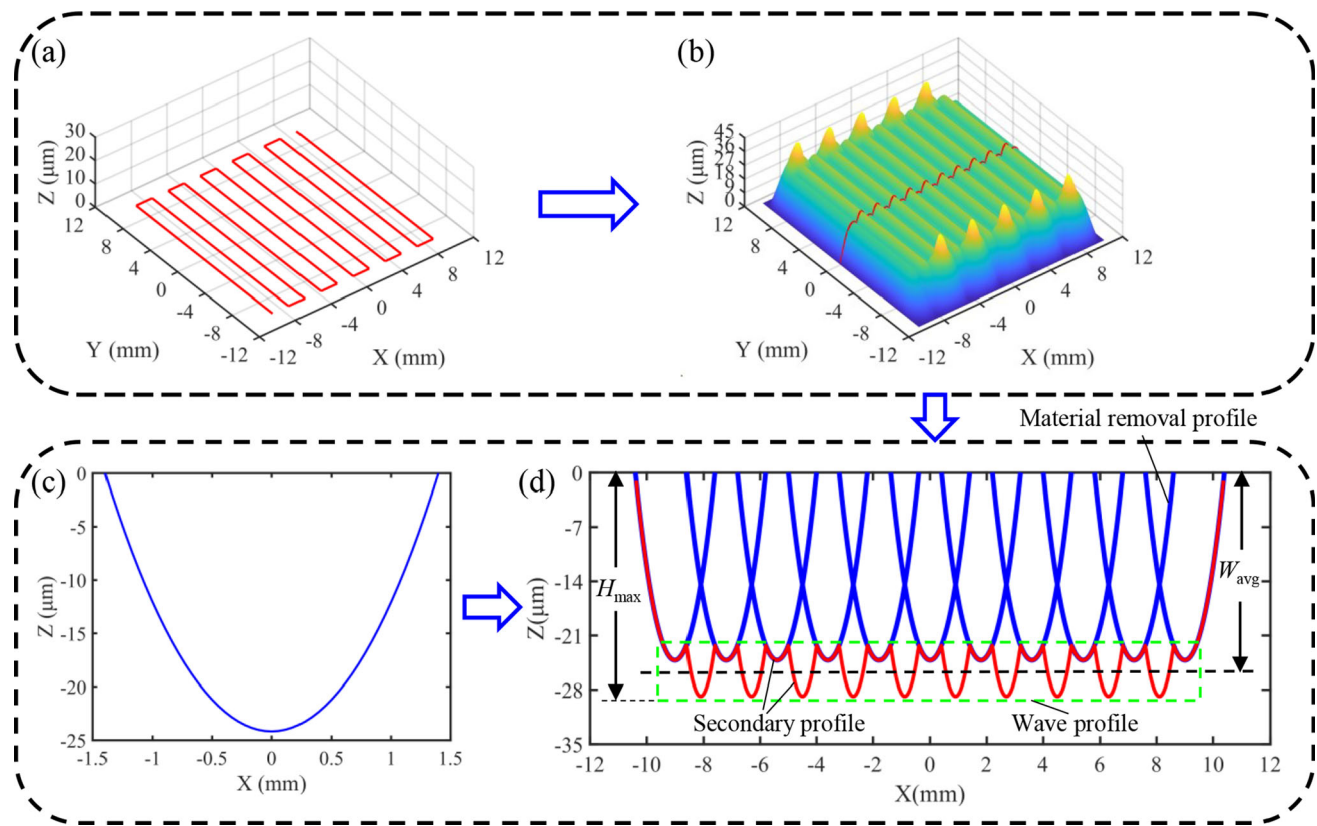**Fig. 7** 3D material removal map: (a) SP and (b) CCP

(a)

(b)
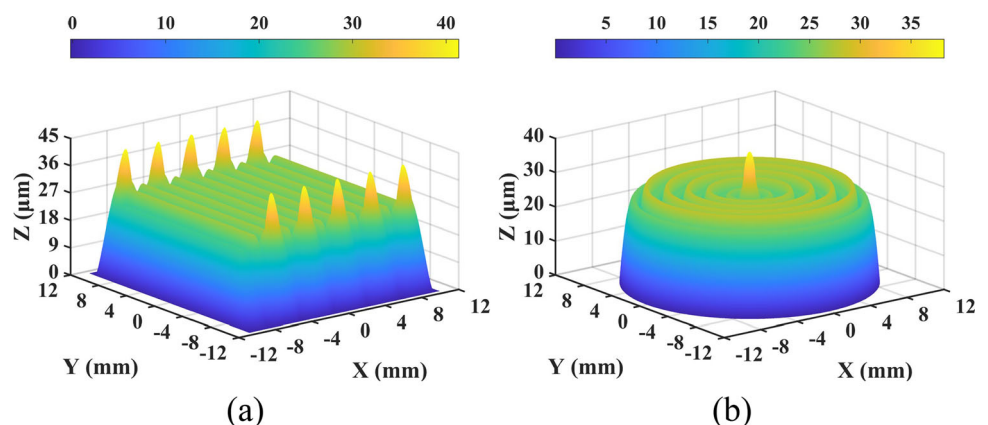
Fig. 8 (a) The scanning path, (b) 3D material removal map, (c) material removal profile, and (d) 2D material removal profile

When m is even, i.e., $m = 2k$, substituting $X = (k-1)s + s/2$ into Eq. 19, the maximum removal depth of H_m can be calculated as

$$(H_m)_{\max}(s, v_a) = \sum_{i=0}^{m-1} h\left(\left((k-1)s + \frac{s}{2}\right) - is, v_a\right) \quad (21)$$

For the nth spacing range, there are $m = n - 1$ and $m = n$. The maximum removal depths of the two secondary profiles are $(H_n)_{\max}$ and $(H_{n-1})_{\max}$ (Fig. 9(a)), respectively. $(H_n)_{\max}$ and $(H_{n-1})_{\max}$ can be calculated by substituting $m = n - 1$ and $m = n$ into Eqs. 20 and 21 respectively, then
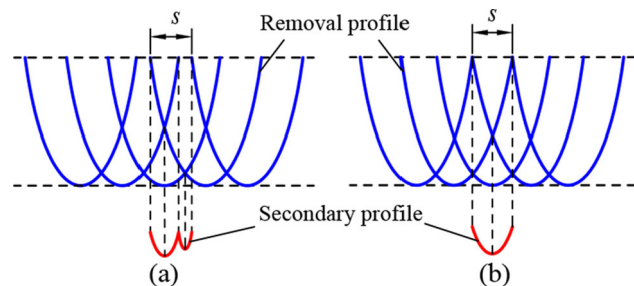
Fig. 9 Overlapping of the material removal profiles in an spacing period s: (a) $s \in (2a/n, 2a/(n-1))$ and (b) $s = 2a/n$

the maximum removal depth of the 2D material removal profile can be calculated as

$$H_{\max} = \min\left((H_n)_{\max}(s, v_a), (H_{n-1})_{\max}(s, v_a)\right) \quad (22)$$

For the nth spacing range, the 2D material removal profile has the minimum removal depth $H_{\min}$ at the junction between the adjacent secondary profiles (Fig. 9(a)). Let $m = n$, and substituting $X = (n-1)s - a$ into Eq. 19, $H_{\min}$ can be calculated as

$$H_{\min} = (H_m)_{\min}(s, v_a) \\ = \sum_{i=0}^{n-1} h\left(((n-1)s - a) - is, v_a\right) \quad (23)$$

As shown in Fig. 8(c), the section of the 2D material removal profile $S(X, s, v_a)$ below $H_{\min}$ is defined as the wave profile $W(X, s, v_a)$, then the range of the wave profile is $a - (N+1)s < X < (N+1)s - a$.

The wave profile is evenly divided into n_w discrete points, and then the average value (W_{avg}), peak-to-valley value (W_{pv}), and standard deviation (W_σ) of the wave profile can be calculated. The W_{pv} value and W_σ value are used to represent the fluctuation amplitude and uniformity of the wave profile, respectively.

The feed velocity of the tool polishing along the straight paths in the inner area and the edge area are v_a and v_{ae}
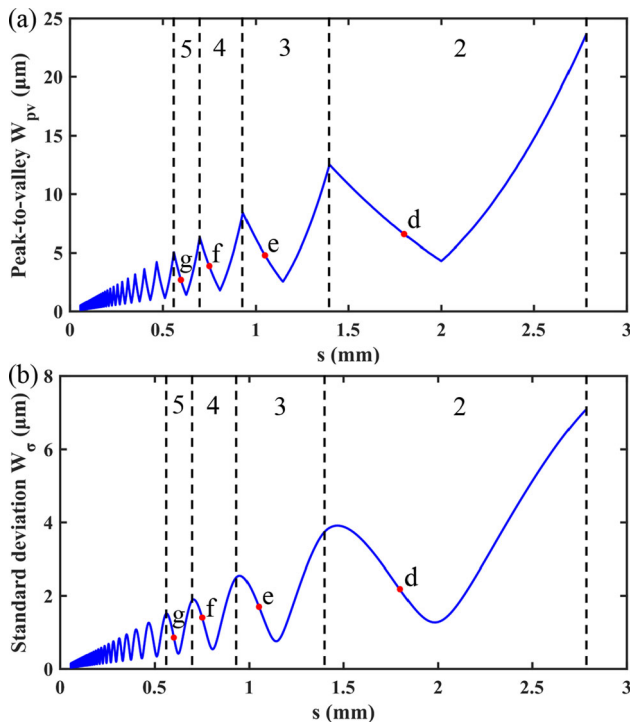
Fig. 10 (a) The W_{pv} plot [23] and (b) W_σ plot for s values between 0 and $2a$

respectively, then the total polishing time of SP can be calculated as

$$T_t = \frac{(2N+1)L_y}{v_a} + \frac{2Ns}{v_{ae}} \tag{24}$$

3.2 Optimization of the material removal uniformity in the inner area

3.2.1 Effect of path spacing s on material removal

The W_{pv} values and W_σ values for spacing s values between 0 and $2a$ have been calculated and plotted (Fig. 10), respectively. From Fig. 10(a) and (b), the W_{pv} plot and W_σ plot are in the shape of a series of "V," and the major trend is that W_{pv} and W_σ decrease with s. Furthermore, each "V" is associated exactly with an spacing range.

SP at s=1.8mm, 1.05mm, 0.75mm, and 0.6mm are recorded as $(SP_2)_1$, $(SP_3)_1$, $(SP_4)_1$, and $(SP_5)_1$, respectively. The locations of the four s values are also labeled in the W_{pv} plot and W_σ plot as points d, e, f, and g, which are associated with the 2nd, 3rd, 4th, and 5th spacing range. For the four paths, the 2D material removal profiles and the evaluation parameters are calculated by simulations. In the simulations, the size of the polishing area is 10×10mm. The parameters of the tool and flat workpiece are listed in Table 1, and the process parameters are listed in Table 2 (in this section, let $v_{ae} = v_a$). The simulation results are

shown in Fig. 11 and listed in Table 3. As shown in Fig. 11, all wave profiles fluctuate periodically, and the part of each wave profile in each fluctuation period s is two secondary profiles with different amplitudes.

For the nth spacing range $s \in (2a/n, 2a/(n-1))$, the maxima of the W_{pv} plot located at $s = 2a/n$ and $s = 2a/(n-1)$, and the minima of the Wpv plot located at $s = s_n$ (s_n represents the spacing associated with the valley of the "V" for the nth spacing range) [23]. Firstly, the wave profile has only one kind of secondary profile at $s = 2a/(n-1)$ [23]. Then, as s decreases, the second secondary profile will appear and gradually increases with respect to the first secondary profile [23]. It seems that the two secondary profiles have the same minima at $s = s_n$ [23]. Finally, at $s = 2a/n$, the first profile disappears and the wave profile once again has only one kind of secondary profile [23]. Therefore, for the nth spacing range, the material removal is the most uniform at $s = s_n$ and the most uneven at $s = 2a/n$ and $2a/(n-1)$. Accordingly, the spacing s_n is the optimal spacing value for the nth spacing range. Tam et al. [23] regarded the removal profile as a parabola and obtained a regular formula for calculating the s_n value. However, the removal profile is a quadratic curve, so there is an error in the s_n value calculated by their method. For this purpose, the s_n value will be precisely calculated in the following section.

3.2.2 Calculation of the optimal spacing value s_n

For a certain s value, the maximum removal depths $(H_n)_{max}$ and $(H_{n-1})_{max}$ of the two secondary profiles can be calculated by Eqs. 20 and 21, respectively. Therefore, the $(H_n)_{max}$ plot and $(H_{n-1})_{max}$ plot for the s value varying in the nth spacing range can be calculated respectively, and the intersection of the two plots just corresponds to the s_n value. The equations of the $(H_n)_{max}$ plot and $(H_{n-1})_{max}$ plot can be obtained respectively by polynomial fitting. Then the s_n value can be obtained by solving the two fitting equations.

Figure 12 shows the polynomial fitting results of the $(H_n)_{max}$ plot and $(H_{n-1})_{max}$ plot for the 2nd to 5th spacing ranges, and the four s_n values are 1.9998mm, 1.1455mm, 0.8084mm, and 0.6257mm respectively. SP at the four s_n values are recorded as $(SP_2)_2$, $(SP_3)_2$, $(SP_4)_2$, and $(SP_5)_2$, respectively. For the four SP, the 2D material removal profiles and the evaluation parameters are shown in Fig. 13 and listed in Table 3 respectively. From Fig. 13(a) to (d), the $(H_n)_{max}$ value and $(H_{n-1})_{max}$ value of the two secondary profiles are consistent. It indicates that the method of calculating the s_n value is valid. Compared with the random s value motioned in Section 3.2.1, the W_{pv} value and W_σ value at $s = s_n$ are significantly reduced, which indicates that the uniformity of material removal has been greatly improved. Moreover, from Table 3, the H_{max} value and T_t

Fig. 11 2D materval removal profile: (a) $(SP_2)_1$; (b) $(SP_3)_1$; (c) $(SP_4)_1$; (d) $(SP_5)_1$
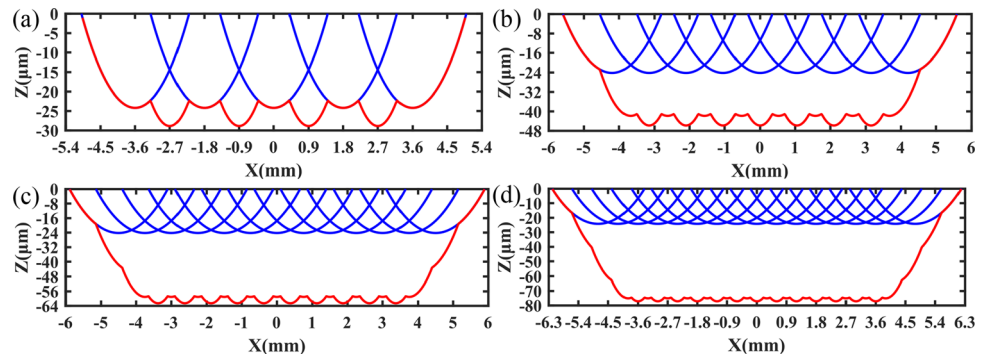
value increases as s decreases. Therefore, it is necessary to optimize the relevant process parameters to make the material removal thickness the given value (h_e) and to ensure polishing efficiency.

3.2.3 Calculation of the feed velocity v_a

The depth of the material removal profile is inversely proportional to the feed velocity v_a. Therefore, the removal depth can be controlled by optimizing the feed velocity v_a. The given material removal thickness is h_e, then substitution of $(H_m)_{\max} = -h_e$ into Eqs. 20 and 21 yields

$$v_a = \begin{cases} \sum_{i=0}^{m-1} h\left(ks - is, -h_e\right), & m = 2k+1 \\ \sum_{i=0}^{m-1} h\left(\left((k-1)s + \frac{s}{2}\right) - is, -h_e\right), & m = 2k \end{cases} \quad (25)$$

Let h_e=0.02mm, the feed velocities v_a optimized by Eq. 25 for s_n=1.9998mm, 1.1455mm, 0.8084mm, and 0.6257mm are 0.0242mm/s, 0.0405mm/s, 0.0569mm/s, and 0.0731mm/s respectively. SP at the four optimized v_a values are recorded as $(SP_2)_3$, $(SP_3)_3$, $(SP_4)_3$, and $(SP_5)_3$, respectively. For the

four SP, the 2D material removal profiles and the evaluation parameters are shown in Fig. 14 and listed in Table 3 respectively. From Table 3, the $H_{\max}$ values at the four optimized v_a values are about 0.02mm. It indicates that the material removal thickness can be precisely controlled by optimizing the feed velocity v_a. In addition, the W_{pv} values and W_σ values at the four optimized v_a values are significantly lower than before optimizing the feed velocity v_a. The improvement in material removal uniformity is due to the reduction in the amplitude of the wave profile caused by the reduction in the $H_{\max}$ value in a certain proportion. Moreover, the T_t values at the four optimized v_a values are close. It shows that although the spacing s_n changes, the polishing efficiency is also guaranteed while the feed velocity v_a is optimized to achieve the same material removal thickness h_e.

3.3 Optimization of the over-polishing in the edge area

It can be seen from Fig. 7(a) that multiple removal peaks with different heights are generated in the edge area of

Table 3 Evaluation parameters for the material removal in the inner area

| Spacing range	Optimizing parameters		$H_{\max}$ (μm)	W_{pv} (μm)	W_σ (μm)	T_t (s)
	s (mm)	v_a (mm/s)				
$a < s < 2a$	1.8	0.02	−28.855	6.597	2.164	2860
	1.9998	0.02	−24.172	4.311	1.293	2900
	1.9998	0.0242	−19.977	3.563	1.069	2397
$2a/3 < s < a$	1.05	0.02	−45.791	4.761	1.718	4920
	1.1455	0.02	−40.55	2.554	0.767	4958
	1.1455	0.0405	−20.025	1.261	0.379	2448
$a/2 < s < 2a/3$	0.75	0.02	−62.56	3.883	1.436	6950
	0.8084	0.02	−56.856	1.814	0.539	6985
	0.8084	0.0569	−19.984	0.638	0.19	2455
$2a/5 < s < 2a/4$	0.6	0.02	−77.1	2.554	0.897	8980
	0.6257	0.02	−73.146	1.409	0.42	7938
	0.6257	0.0731	−20.013	0.386	0.115	2172

Fig. 12 The $(H_n)_{max}$ plot and $(H_{n-1})_{max}$ plot: (a) the 2nd spacing range; (b) the 3rd spacing range; (c) the 4th spacing range; (d) the 5th spacing range
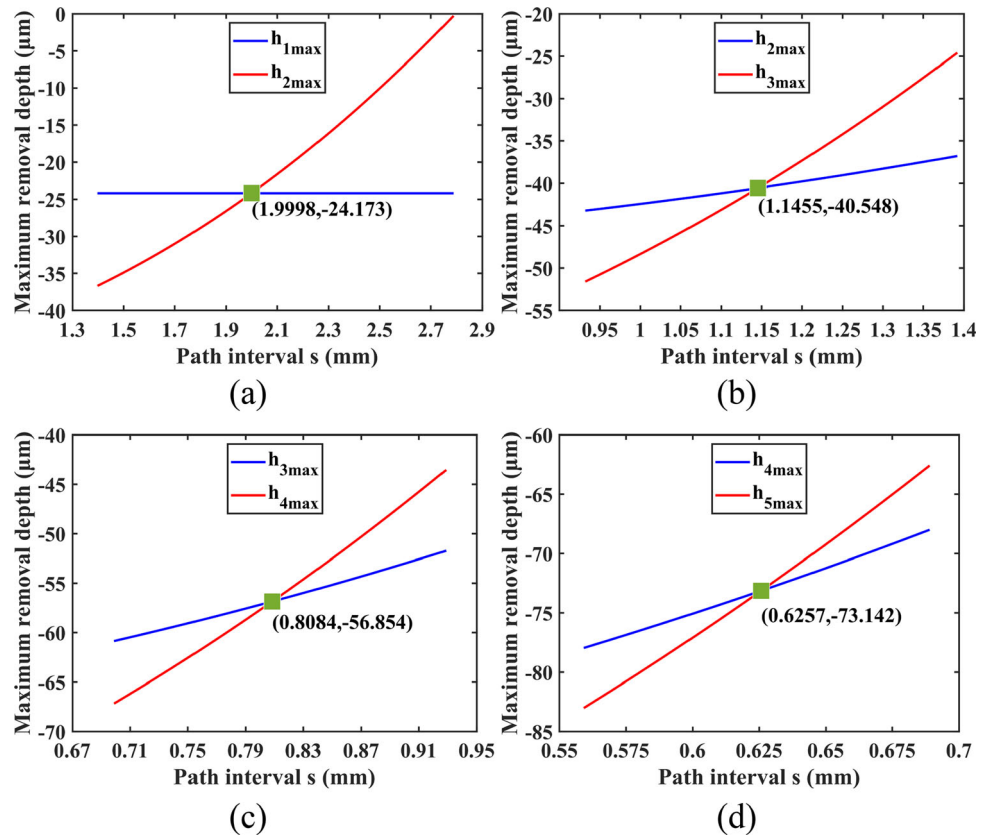
Fig. 13 2D materval removal profile: (a) $(SP_2)_2$; (b) $(SP_3)_2$; (c) $(SP_4)_2$; (d) $(SP_5)_2$
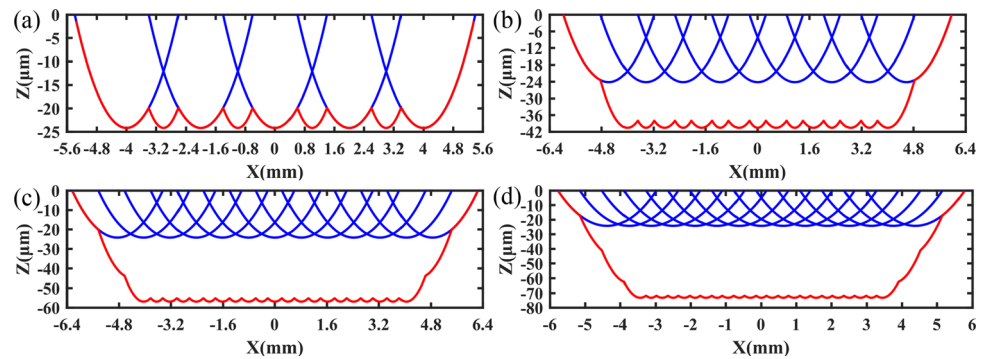
Fig. 14 2D materval removal profile: (a) $(SP_2)_3$; (b) $(SP_3)_3$; (c) $(SP_4)_3$; (d) $(SP_5)_3$
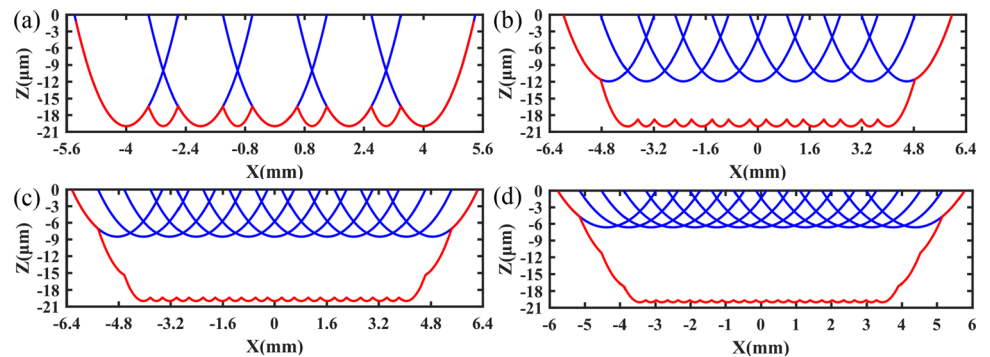
SP, which are arranged in a periodic linear along the edge area. This is the over-polishing phenomenon caused by the alternation of the short straight paths in the edge area, which is urgently needed to be optimized.

Firstly, the influencing factors of the over-polishing in the edge area are analyzed here. Given that the matrix of the global material removal is M_s, the maximum removal depth in the edge area can be calculated by MATLAB as

$$E_{\max} = \min(M_s) \tag{26}$$

Then the peak-valley value of the material removal depth in the edge area can be calculated as [23]

$$E_{pv} = H_{\min} - E_{\max} \tag{27}$$

The ratio of the $E_{\max}$ value to the $H_{\max}$ value is defined as r_{e1}, and the ratio of the E_{pv} value to the W_{pv} value is defined as r_{e2} [23]. r_{e1} and r_{e2} are used to describe the degree of the over-polishing in the edge area, which can be expressed as

$$r_{e1} = \frac{E_{\max}}{H_{\max}}, r_{e2} = \frac{E_{pv}}{W_{pv}} \tag{28}$$

For $(SP_2)_3$, $(SP_3)_3$, $(SP_4)_3$, and $(SP_5)_3$, the 3D material removal maps and the evaluation parameters are shown in Fig. 15 and listed in Table 4 respectively. From Table 4, the E_{pv} value, r_{e1} value, and r_{e2} value decrease with the spacing

s_n. It indicates that the over-polishing in the edge area is gradually alleviated as the s value decrease.

Due to the material removal depth in the edge area is directly related to the feed velocity v_{ae}, the over-polishing in the edge area can be improved by optimizing the feed velocity v_{ae}. For SP at $s=1.9998$mm and $v_a=0.0242$mm/s, the E_{pv} values, r_{e1} values, and r_{e2} values for the feed velocity v_{ae} varying from 0.01 to 2mm/s have been calculated and plotted (Fig. 16). As shown in Fig. 16(a) and (b), the E_{pv} value, r_{e1} value, and r_{e2} value are first dropped sharply and then tend to be smooth as the feed velocity v_{ae} increase.

The four SP at $v_{ae}=10$mm/s are recorded as $(SP_2)_4$, $(SP_3)_4$, $(SP_4)_4$, and $(SP_5)_4$, respectively. For the four SP, the 3D material removal maps and the evaluation parameters are shown in Fig. 17 and listed in Table 4 respectively. From Table 4, after optimizing the feed velocity v_{ae}, the E_{pv} value is significantly reduced, and the r_{e1} value and r_{e2} value are almost equal to 1. It indicates that the over-polishing in the edge area can be significantly eliminated by optimizing the feed velocity v_{ae}. In addition, after optimizing the feed velocity v_{ae}, the T_t value also decreases slightly, that is, the polishing efficiency is improved. Therefore, to eliminate the over-polishing in the edge area and improve polishing efficiency, the feed velocity v_{ae} should be set as high as possible.

Fig. 15 3D material removal map when $v_{ae}=v_a$: (a) $(SP_2)_3$; (b) $(SP_3)_3$; (c) $(SP_4)_3$; (d) $(SP_5)_3$
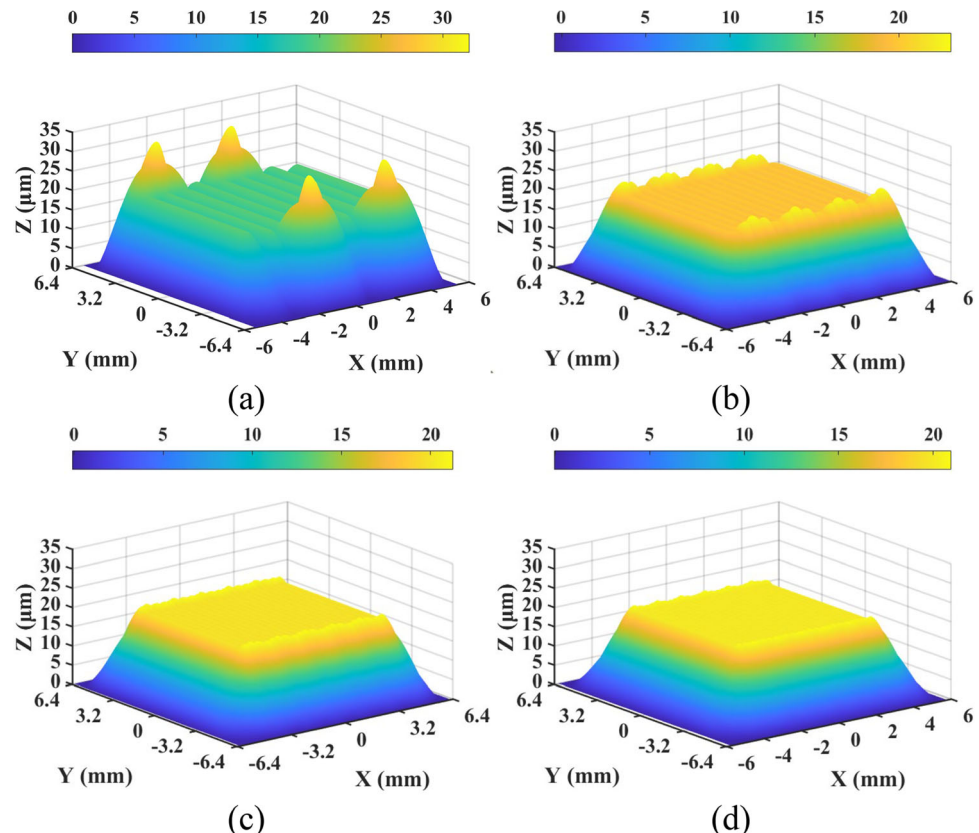
Table 4 Evaluation parameters for the material removal in the edge area

Spacing range	Optimizing parameters			E_{max} (μm)	E_{pv} (μm)	r_{e1} (μm)	r_{e2} (μm)	T_t (s)
	s (mm)	v_a (mm/s)	v_{ae} (mm/s)					
$a < s < 2a$	1.9998	0.0242	0.0242	−32.118	15.704	1.608	4.408	2397
	1.9998	0.0242	10	−20.001	3.587	1.001	1.007	2067
$2a/3 < s < a$	1.1455	0.0405	0.0405	−23.088	4.325	1.153	3.429	2448
	1.1455	0.0405	10	−20.033	1.269	1	1.006	2223
$a/2 < s < 2a/3$	0.8084	0.0569	0.0569	−21.256	1.909	1.064	2.993	2455
	0.8084	0.0569	10	−19.988	0.641	1	1.006	2286
$2a/5 < s < a/2$	0.6257	0.0731	0.0731	−20.951	1.324	1.047	3.434	2172
	0.6257	0.0731	10	−20.014	0.387	1	1.005	2057

4 Analysis and optimization of the concentric circle path

The concentric circle path is divided into the peripheral area and central area here. Due to the change of the path curvature [18], the material removal profile is not constant throughout the workpiece surface, which leads to the fact that the path spacing law of SP cannot be fully applied to CCP. For CCP, the cross-section of the 3D material removal map is the 2D material removal profile. The process parameters along every single circular path are constant. Due to the rotational symmetry of CCP, the global material removal distribution can be represented by the 2D material

Fig. 16 (a) The E_{pv} plot, (b) r_{e1} plot and r_{e2} plot for v_a between 0.01 and 2mm/s

removal profile. In this section, the 2D material removal profile is first calculated to reveal the material removal uniformity and material removal depth. Then the uniformity of the material removal in the peripheral area will be improved by optimizing the path spacing and process parameters. Lastly, the over-polishing in the central area of CCP will be eliminated by optimizing the central circular path and the process parameters.

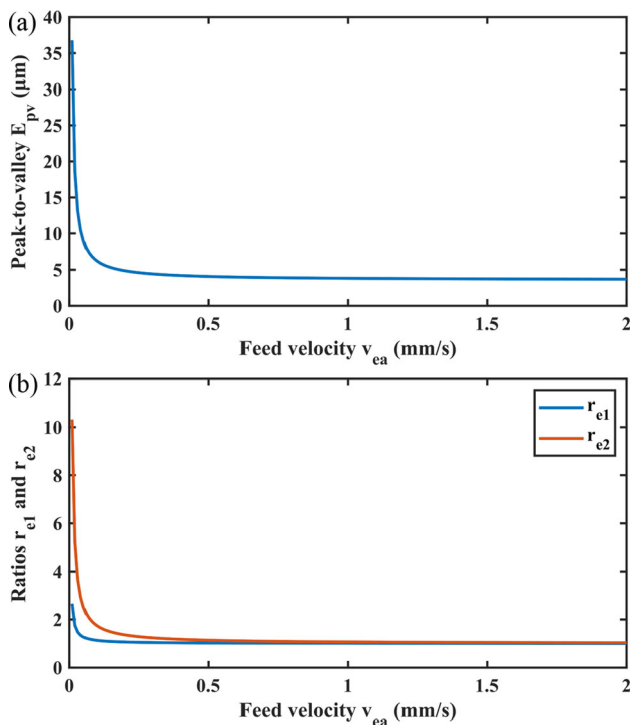## 4.1 2D material removal profile and related calculations

As shown in Fig. 18(a), O is the center point of CCP, the coordinate system $\{O; X, Y, Z\}$ is fixed on the surface at point O, and CCP is located on plane XOY. P_1 is the central circular path of CCP. P_i represents the ith circular path of CCP, and R_i represents the radius of the path P_i, where $i \in (1, N)$. If the radius of the circular area on workpiece surface needs to be polished is R_w, the total number N of the circular paths composed CCP should satisfy the relationship $R_1 + (N − 1)s < R_w < R_1 + Ns$.

The section profile of the 3D material removal map (Fig. 18(b)) along plane XOZ is the 2D material removal profile (Fig. 18(c)). The depth of the 2D material removal profile is taken as the negative value. The 2D material removal profile can be obtained by overlapping the material removal profiles associated with the circular paths, which can be expressed as

$$S(X, s, \delta, v_a) = \sum_{i=1}^{N} h_i(X) \tag{29}$$

where $h_i(X)$ denotes the removal profile associated with the path P_i, when $i = 1$, it is denoted by Eq. 17, and when $i \neq 1$, it is denoted by Eq. 4. The 2D material removal profile S can be seen as the function of the coordinate X, path spacing s, inclination angle δ, and feed velocity v_a.

The optimization of CCP aims to improve the material removal uniformity in the peripheral area and eliminate the

Fig. 17 3D material removal map when v_{ae}=10mm/s: (a) $(SP_2)_4$; (b) $(SP_3)_4$; (c) $(SP_4)_4$; (d) $(SP_5)_4$
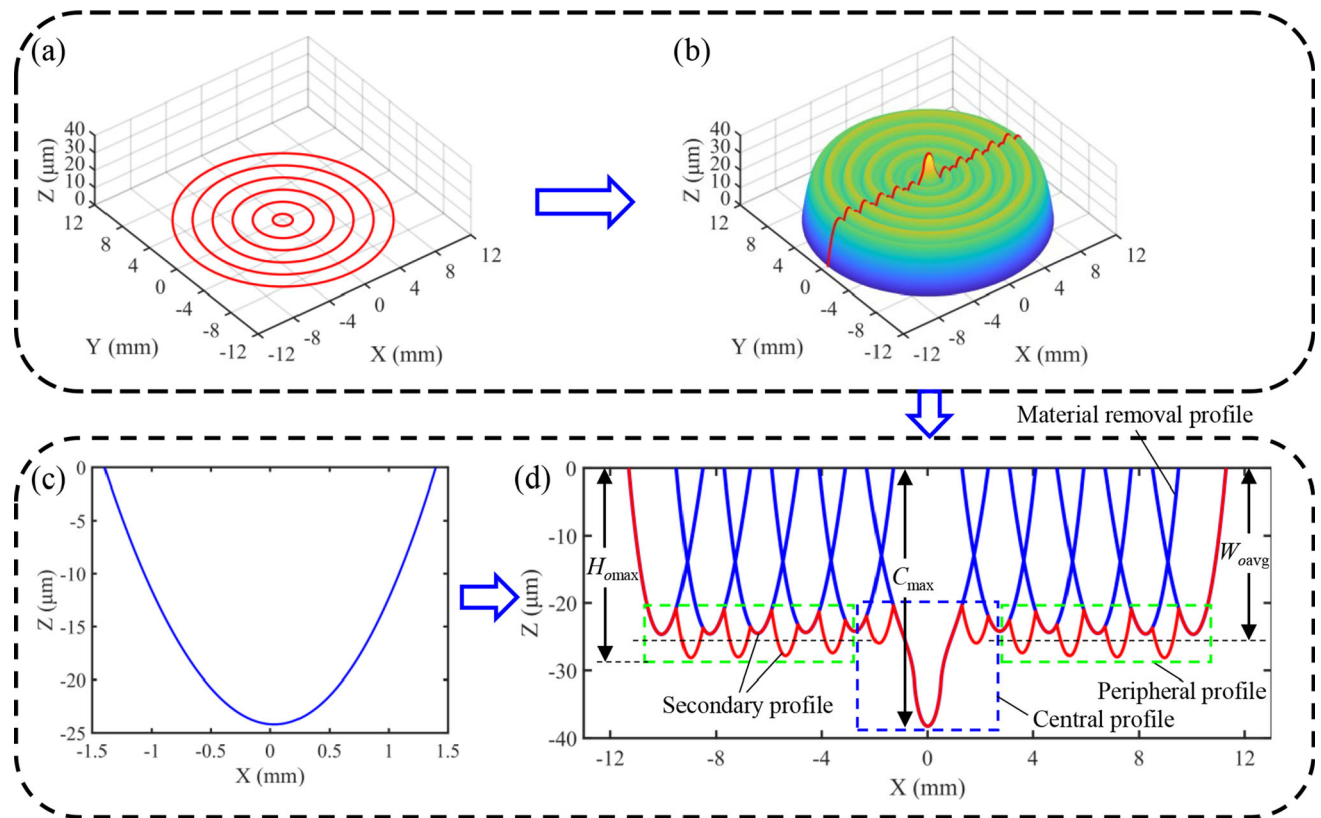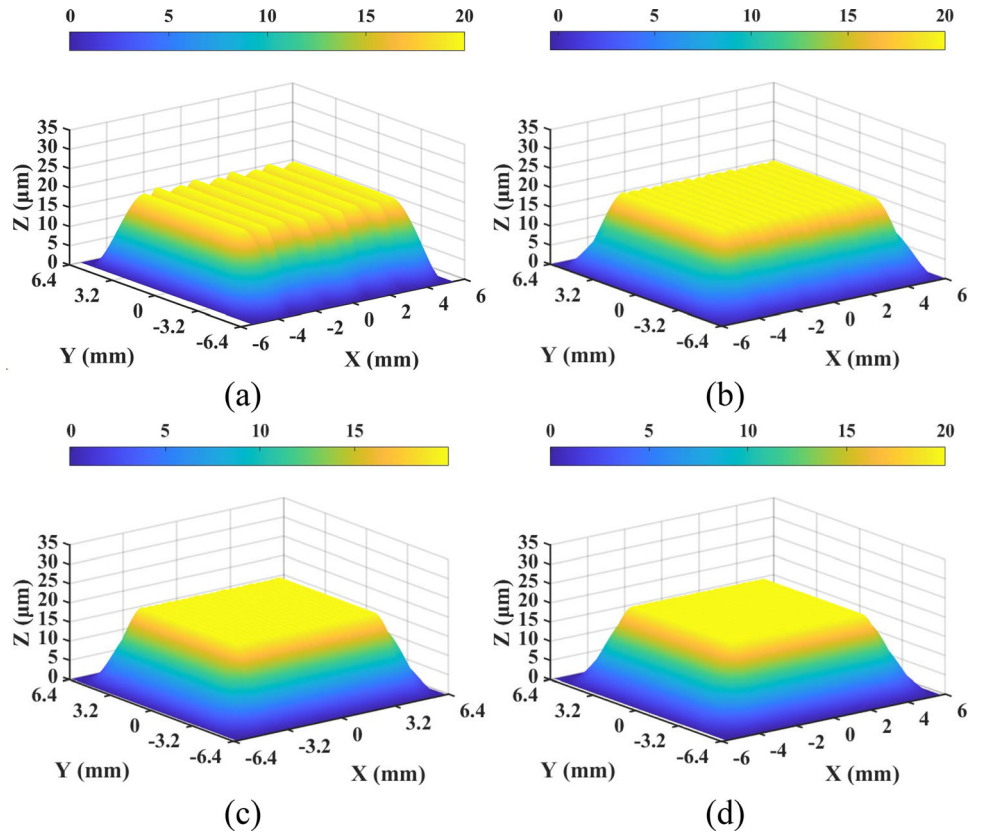
Fig. 18 (a) The concentric circle path, (b) 3D material removal map, (c) material removal profile, and (d) 2D material removal profile

over-polishing in the central area. Therefore, the 2D material removal profile is divided into the peripheral profile W_o and the central profile C. The abscissa range of the peripheral profile W_o is $(R_1 + a) < X < (R_1 + ns)$, and the abscissa range of the central profile C is $-(R_1 + a) < X < (R_1 + a)$. Accordingly, the wave profile can be expressed as

$$W(X, s, \delta, v_a) = C(X, s, \delta, v_a) + W_o(X, s, \delta, v_a),$$
$$-(R + a) < X < R + Ns \qquad (30)$$

where

$$\begin{cases} C(X, s, \delta, v_a) = \sum_{i=1}^{2} h_i(X), -(R + a) < X < R + a \\ W_o(X, s, \delta, v_a) = \sum_{i=2}^{N} h_i(X), R + a < X < R + Ns \end{cases} \qquad (31)$$

The wave profile is evenly divided into n_w discrete points. and X_i represents the abscissa of the ith discrete point. The maximum value $C_{\max}$, peak-valley value C_{pv}, and standard deviation C_σ of the central profile C and the maximum value $H_{o\max}$, average value (W_{oavg}), peak-valley value W_{opv}, and standard deviation $W_{o\sigma}$ of the peripheral profile W_o can be calculated.

The ratio of $C_{\max}$ to $H_{o\max}$ is defined as r_{c1}, and the ratio of C_{pv} to W_{opv} is defined as r_{c2}. r_{c1} and r_{c2} are used to describe the degree of over-polishing in the central area of CCP, which can be expressed as

$$r_{c1} = \frac{C_{\max}}{H_{o\max}}, r_{c2} = \frac{C_{pv}}{W_{opv}} \qquad (32)$$

4.2 Optimization of the material removal uniformity in the peripheral area

CCP mentioned in Section 2.3 is recorded as $(CCP_2)_1$. For path $(CCP_2)_1$, the 2D material removal profile and the evaluation parameters are shown in Fig. 19(a) and listed in Table 5 respectively. As shown in Fig. 19(a), the material removal profiles in the peripheral area are skewed due to the influence of the path curvature [18] and polishing posture [19]. Furthermore, the path curvature variation will lead to the variation of the material removal profile [18]. However, since the curvature of CCP in the simulation changes relatively small, the variation of the material removal profile in the peripheral area is subtle and not easy to be observed. The secondary profile is related to the adjacent removal profile and the spacing between the adjacent paths. Therefore, in Fig. 19(a), there are obvious differences among the secondary profiles due to the unreasonable path spacing and the material removal profile variation in the peripheral area, which leads to the large fluctuation of the peripheral profile. If the material removal profiles in the peripheral area are optimized to be centrally symmetric and have a consistent maximum removal depth, the difference among the removal profiles can be ignored. At this time, the spacing law of CCP may be applied to SP, and the uniformity of the peripheral profile may be significantly improved. Therefore, it is necessary to optimize the process parameters so that the material removal profile in the peripheral area is center-symmetric and its maximum removal depth is the given value h_e.

According to the research of Fan et al. [19], the centrosymmetric material removal profile can be obtained by optimizing the polishing posture angles. The material removal profile is not only a function of ρ but also a function of δ and λ. Therefore, the optimization of polishing posture angles δ and λ can be expressed as [19]

$$F(\lambda, \delta) = \frac{\partial h(\lambda, \delta, \rho)}{\partial \rho}\bigg|_{\rho = R} = 0 \qquad (33)$$

Equation (33) can be numerically calculated by the backward difference formula and the calculation is formulated as an optimization problem, as written below [19]

$$\min |F(\lambda, \delta)| \approx \min \left| \frac{h(R) - h(R - \Delta\rho)}{\Delta\rho} \right| \qquad (34)$$
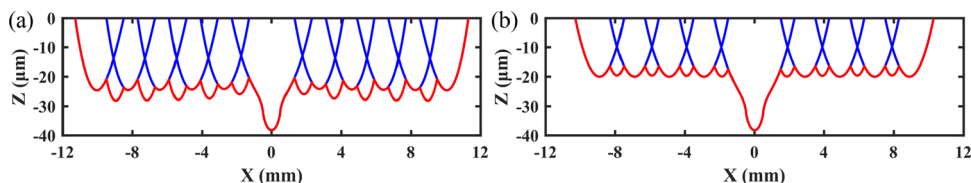
where $\Delta\rho$ is the increment. When optimizing the polishing posture angles, the declination angle $\lambda(\lambda$ is set as 0 in this paper) is first set, and then the inclination angle δ is calculated by Eq. 34.

After the inclination angle δ has been optimized, substituting $h(R) = -h_e$ into Eq. 4, the feed velocity v_a can be calculated as

$$v_a = \frac{3K_p F_n \omega R}{2\pi h_e a^3} \int_{-\arccos\left(\frac{R^2 + R - a^2}{2R^2}\right)}^{\arccos\left(\frac{R^2 + R - a^2}{2R^2}\right)} f(R, \theta) d\theta \qquad (35)$$

For CCP at $s = 1.9998$mm, let $\lambda = 0^o$ and $h_e = 0.02$mm, the inclination angle δ and feed velocity v_a in the peripheral area were optimized by Eqs. 34 and 35 respectively. The optimized results are shown in Fig. 20. CCP at $s = 1.9998$mm after optimizing δ and v_a in the peripheral area is recorded as $(CCP_2)_2$. For path $(CCP_2)_2$, the 2D

Fig. 19 2D material removal profile: (a) $(CCP_2)_1$; (b) $(CCP_2)_2$

Table 5 Evaluation parameters for the material removal in the peripheral area

| | Optimizing parameters | | | | | |
States	s (mm)	δ (°)	v_a (mm/s)	$E_{\max}$ (μm)	W_{opv} (μm)	$W_{o\sigma}$ (μm)
Not optimized	1.8	30	0.02	−28.134	7.321	1.892
Optimized δ, v_a, and s	1.9998	Fig. 20(a)	Fig. 20(b)	−20	3.676	1.064

material removal profiles and the evaluation parameters are shown in Fig. 19(b) and listed in Table 5 respectively. From Fig. 19(b), after optimizing δ and v_a, the material removal profiles in the peripheral area are center-symmetric and have the consistent maximum removal depth h_e. Compared with the peripheral profile in Fig. 19(a), the fluctuation of the peripheral profile in Fig. 19(b) is more uniform. As shown in Table 5, compared with path $(CCP_2)_1$, the W_{opv} value and $W_{o\sigma}$ value for path $(CCP_2)_2$ are reduced by 49.8% and 47.8%, respectively. In addition, the $H_{o\max}$ value for path $(CCP_2)_2$ is 0.02mm. It can be known from the above analysis that the path spacing law of SP can be effectively applied to CCP after optimizing the material removal profile in the peripheral area.

4.3 Optimization of the over-polishing in the central area

The key to eliminating the over-polishing in the central area lies in how to optimize the material removal profile h_1 associated with the central circular path P_1 and the spacing s_1 between path P_1 and path P_2.

Figure 21(a) shows the theoretical removal profiles h_1 for R_1 varying from 0 to $a/2$ (where R_1 is the radius of path P_1 and a=1.3977mm in this paper). Figure 21(b) shows the theoretical material removal profiles h_1 for R_1 varying from

(a)

(b)

Fig. 20 Optimized process parameters: (a) inclination angle and (b) feed velocity

$a/2$ to a. From Fig. 21(b), when $R_1 \in (a/2, a)$, the material removal profile h_1 has three secondary profiles, and the left and right secondary profiles are the same. Figure 22 is the schematic diagram of the material removal profile h_1 when $R_1 \in (a/2, a)$. In Fig. 22, the secondary profile in the middle is h_{11}, and the secondary profile on both sides is h_{12}. $h_{11\max}$ and $h_{12\max}$ are the maximum removal depths of h_{11} and h_{12}, respectively. First, R_1 needs to be optimized to make $h_{11\max} = h_{12\max}$ to reduce the fluctuation of the material removal profile h_1.

When $R_1 \in (a/2, a)$, the depth of the material removal profile h_1 at $\rho = R_1$ can be calculated by Eq. 16. At this time, the inclination angle δ_1 for path P_1 can be optimized by Eq. 34. After optimizing δ_1, the secondary profile h_{12} has the maximum removal depth $h_{12\max}$ at $\rho = R_1$. Furthermore, $h_{11\max}$ can be calculated by substituting $\rho = 0$ into Eq. 15. Therefore, for the case of $R_1 \in (a/2, a)$, after optimizing δ_1 by Eq. 34, $h_{11\max}$ and $h_{12\max}$ can be calculated as

$$\begin{cases} h_{11\,\max} = h_\gamma\,(0) \\ h_{12\,\max} = h_\zeta\,(R_1) \end{cases} \tag{36}$$

Next, the $h_{11\max}$ plot and $h_{12\max}$ plot for R_1 varying from $a/2$ to a can be calculated by Eq. 36 are shown in Fig. 23(a). The $h_{11\max}$ plot and $h_{12\max}$ plot intersect at two points (q and u). To solve points q and u, the equations of the $h_{11\max}$ plot and $h_{12\max}$ plot for R_1 varying from 0.9 to 1.2mm are obtained respectively by polynomial fitting. Then points q and u can be obtained by solving the two fitting equations. Figure 23(b) shows the polynomial fitting results. There are R_1=0.9694mm and $\delta_1 = 13.822^o$ and R_1=1.0773mm and $\delta_1 = 15.572^o$ at points q and u respectively.

The material removal profiles h_1 at points q and u are shown in Fig. 24a and b respectively. From Fig. 24a and b, the two material removal profiles h_1 both satisfy $h_{11\max} = h_{12\max}$. Then, $h_{11\max}$ and $h_{12\max}$ need to be adjusted to being the given material removal thickness (h_e) by optimizing the feed velocity v_{a1} for path P_1. Substituting $h(0) = -h_e$ into Eq. 15, the feed velocity v_{a1} can be calculated as

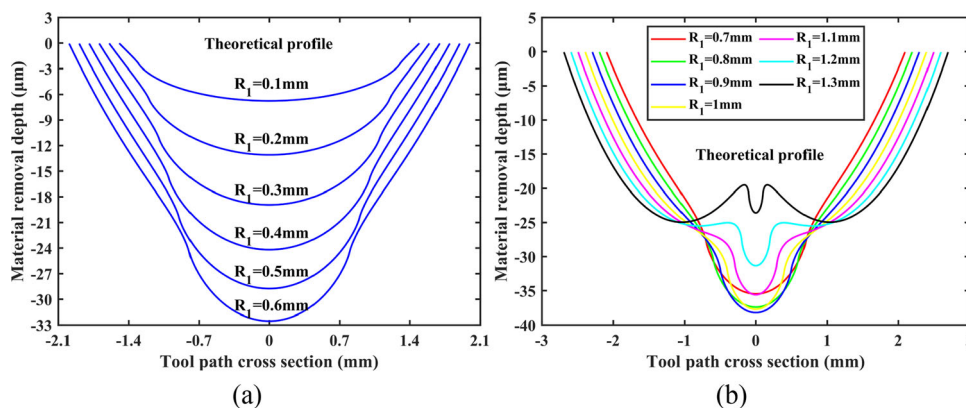$$v_{a1} = \frac{3K_p F_n \omega R}{2\pi h_e a^3} \int_{-\pi}^{\pi} f\,(0, \theta)\,d\theta \tag{37}$$

Let h_e=0.02mm, the feed velocities v_{a1} at points q and u optimized by Eq. 37 are 0.0115mm/s and 0.013mm/s respectively. Next, the spacing s_1 can be approximated taken
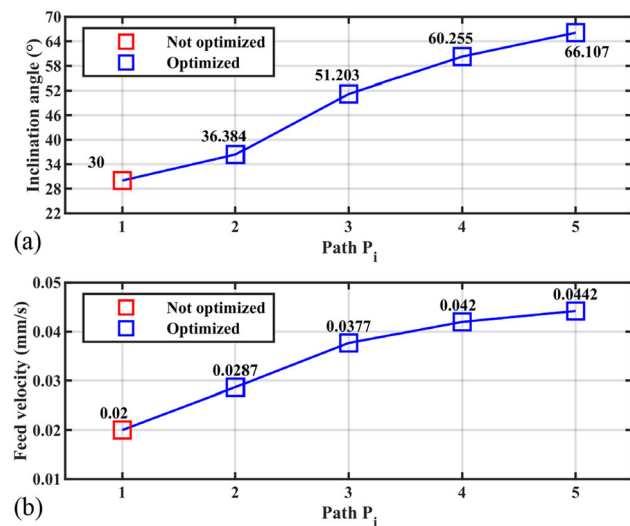
Fig. 21 Material removal profile h_1: (a) $0 < R_1 < a/2$ and (b) $a/2 < R_1 < a$

as as s_1=1.9998mm. In addition, since the radius of the central path has changed, the radius of the remaining paths will also change accordingly. Thus, the inclination angle and feed velocity of each path need to be re-optimized by Eqs. 34 and 35 respectively.

CCP at points q and u are recorded as $(CCP_2)_3$ and $(CCP_2)_4$ respectively. For the two paths, the 2D material removal profiles and the evaluation parameters are shown in Fig. 25 and listed in Table 6, respectively. The optimized inclination angle and feed velocity are shown in Fig. 26(a) and (b), respectively. From Fig. 25, the uniformity of the center profile is significantly improved after the above optimization. Compared with path $(CCP_2)_2$, the C_{pv} value, C_σ value, r_{c1} value, and r_{c2} value for path $(CCP_2)_3$ are reduced by 83.1%, 84.8%, 46.5%, and 47.2%, respectively. Compared with path $(CCP_2)_2$, the C_{pv} value, C_σ value, r_{c1} value, and r_{c2} value for path $(CCP_2)_4$ are reduced by 83.1%, 84.8%, 81.7%, and 82.7%, respectively. In addition, the C_{max} values for paths $(CCP_2)_3$ and $(CCP_2)_4$ are both 0.02mm. The simulation results show that the

over-polishing in the central area of CCP can be significantly eliminated by optimizing the radius R_1 of the central circular path, the spacing s_1, inclination angle δ_1, and feed velocity v_{a1}.
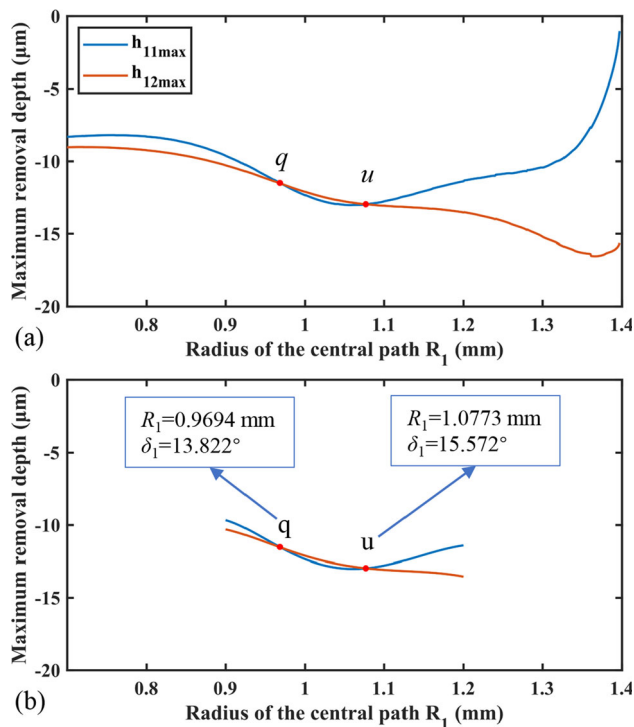
5 Polishing experiments

5.1 Experimental conditions

A series of experiments were conducted to verify the validity of the models and methods proposed in this paper. The five-axis CNC machine tool used in the experiment is
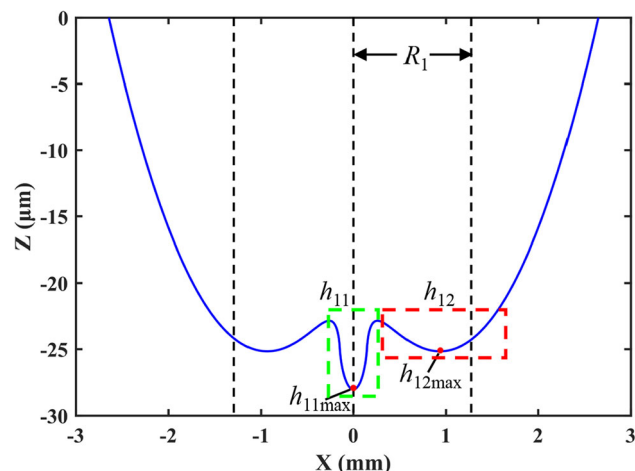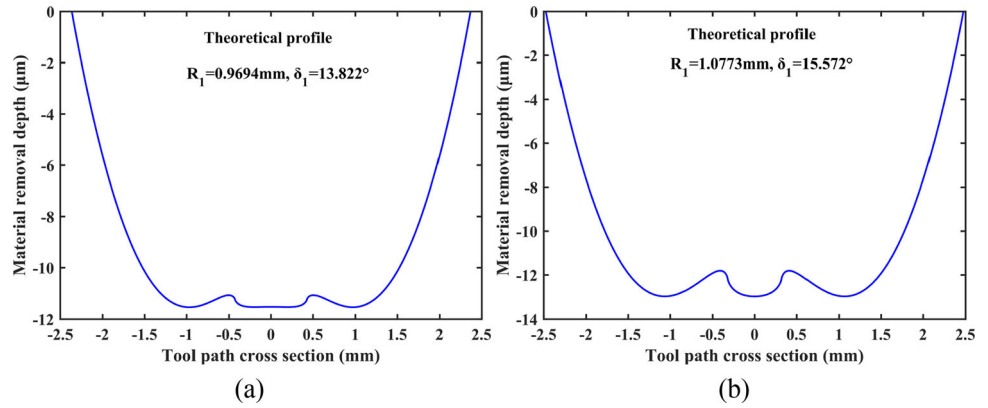

Fig. 22 Schematic of material removal profile h_1

Fig. 23 The h_{11max} plot and h_{12max} plot for R_1 between 0 and a: (a) original plots and (b) fitted plots

Fig. 24 Material removal profile h_1: (a) R_1=0.9694mm and $\delta_1 = 13.822^o$ and (b) R_1=1.0773mm and $\delta_1 = 15.572^o$

shown in Fig. 27(a), which is equipped with three linear axes X, Y, and Z, and two rotary axes B and C. The linear axis X, Y, and the rotary axis C realize the movement and rotation of the workpiece, and the linear axis Z and the rotary axis B realize the movement and swing of the tool head. Five-axis linkage realizes the polishing process (Fig. 27(b)). The surface roughness and the surface profile of the workpiece were measured by the Taylor profiler shown in Fig. 28(a).

In the experiments, the tool is spherical polyurethane with a radius of 8mm, and the flat workpiece is made of K9 glass. The parameters of the tool and the workpiece are listed in Table 1. The polishing slurry is a mixture of water and CeO_2 with a volume concentration of 0.5%. Figure 27(c) shows the unpolished K9 glass workpiece. The surface roughness and the profile tolerance of the unpolished K9 glass workpiece are 1.2532μm and 12.309μm, respectively. The polishing experiments are divided into three parts, which are the verification experiments for the material removal models, the polishing experiments along SP, and the polishing experiments along CCP.

5.2 Verification experiments of special material removal model

The experiments were conducted to verify the material removal models proposed in Section 2. The polishing paths are straight paths with lengths of 5mm and 2mm, and a circular path with a radius of 1.2mm, which are used to validate Eqs. 10, 14, and 17, respectively. The process parameters are listed in Table 2. The simulation and

experimental results are shown in Fig. 29. The experimental results are consistent with the simulation results, which indicate that the material removal models proposed in Section 2.2 are valid.

5.3 Polishing experiments along the scanning path

The experiments polishing along SP were divided into two groups. The first group experiments were conducted to verify the feasibility of the optimization method of SP proposed in Section 3, and the second group experiments were conducted to verify the influence of different spacing ranges on the material removal uniformity analyzed in Section 3. In the experiments, the polishing paths were derived from the simulations in Section 3 but expanded here to polish a 20×20mm square area. The process parameters are the same as those in the simulations in Section 3.

5.3.1 The first group of experiments

In the experiments, three workpieces were polished along SP with the spacings in the 2nd spacing range. The workpieces polished by paths $(SP_2)_1$, $(SP_2)_2$, and $(SP_2)_4$ were recorded as A1, A2, and A3, respectively. To analyze the material removal in the inner area, the X-axis of SP is selected as the measuring path a, and the surface profile and surface roughness of the workpiece were obtained by the profiler measuring along path a. To analyze the material removal in the edge area, the middle line between the straight path P_0 and the adjacent path P_1 is selected as the measuring path b, and the surface profile of the workpiece was obtained by the profiler measuring along path b.

Fig. 25 2D material removal profile: (a) $(CCP_2)_3$ and (b) $(CCP_2)_4$
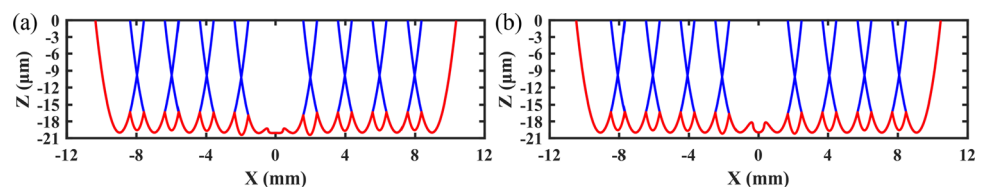
Table 6 Evaluation parameters for the material removal in the central area

States	Optimizing parameters			C_{max} (μm)	C_{pv} (μm)	C_σ (μm)	r_{c1}	r_{c2}
	δ_1 (°)	v_{a1} (mm/s)	R_1 (mm)					
Not optimized	30	0.02	0.9	−38.208	21.777	7.006	1.91	5.925
Point q	13.822	0.0115	0.9694	−20	3.676	1.064	1.021	1.087
Point u	15.572	0.013	1.0773	−20	3.676	1.064	1.009	1.025

Figure 28(b) shows the measuring process. The measured results of the surface profiles are shown in Fig. 30. The evaluation parameters of the surface profiles are calculated and shown in Table 7.

Compared with Fig. 30(a), the surface profile in Fig. 30(c) is more gentle. According to Table 7, the W_{pv} values for workpieces A1 and A2 are 9.767μm and 6.500μm, and the W_σ values for workpieces A1 and A2 are 2.562μm and 1.517μm, respectively. The reductions in the W_{pv} value and W_σ value show that the path spacing optimization method proposed in Section 3.2.2 can effectively improve the material removal uniformity. According to Fig. 30(c) and (e), the H_{max} values for workpieces A1 and A3 are −32.765μm and −22.688μm respectively. The error between the H_{max} value of path workpiece A3 and the given removal thickness (−20μm) is only 10%. It indicates that the optimization method of feed velocity v_a proposed in Section 3.2.2 can control the material removal thickness. The surface roughness R_a of workpieces A1 and A3 are 0.0561μm and 0.0486μm respectively. The reduction in surface roughness shows that the surface quality is improved with the improvement of material removal uniformity. It can be seen from Fig. 30(b) and (d) that there is obvious over-polishing in the edge area of SP. Compared with Fig. 30(b)

and (d), the surface profile in Fig. 30f is more gentle. The E_{pv} values for workpieces A2 and A3 are 21.681μm and 4.898μm, and the r_{e1} values for workpieces A2 and A3 are 1.529 and 1.039, respectively. The reductions in the E_{pv} value and r_{e1} value show that the optimization method of feed velocity v_{ae} proposed in Section 3.3 can effectively eliminate the over-polishing on the edge area.

5.3.2 The second group of experiments

In the experiments, three workpieces were polished along SP with the spacings in the 3rd, 4th, and 5th spacing range. The workpiece polished by paths $(SP_3)_4$, $(SP_4)_4$, and $(SP_5)_4$ are recorded as B1, B2, and B3, respectively. The surface roughness and surface profile of the workpiece were obtained by the profiler measuring along path a. The measured results of the surface profiles are shown in Fig. 31. The evaluation parameters of the surface profiles are calculated and shown in Table 8.

The W_{pv} values for workpieces B1, B2, and B3 are 1.594μm, 1.035μm, and 0.838μm, and the W_σ values for workpieces B1, B2, and B3 are 0.252μm, 0.177μm, and 0.126μm, respectively. The reductions in the W_{pv} value and W_σ value show that the material removal uniformity is improved with the decrease of the optimal spacing value s_n. The surface roughness R_a of workpieces B1, B2, and B3 are 0.0403μm, 0.0382μm, and 0.0370μm respectively. The reduction in surface roughness shows that the surface quality is improved with the improvement of material removal uniformity. Based on the above analysis, when planning the polishing path spacing, the appropriate spacing can be selected according to the desired profile accuracy of the workpiece surface by the method proposed in this paper.

5.4 Polishing experiments along the concentric circle path

The experiments were conducted to verify the feasibility of the optimization method of CCP proposed in Section 4. In the experiment, three workpieces were polished. The workpiece was polished by the paths $(CCP_2)_1$, $(CCP_2)_2$, and $(CCP_2)_3$ are recorded as C1, C2, and C3, respectively. The polishing area is a circular area with a diameter of
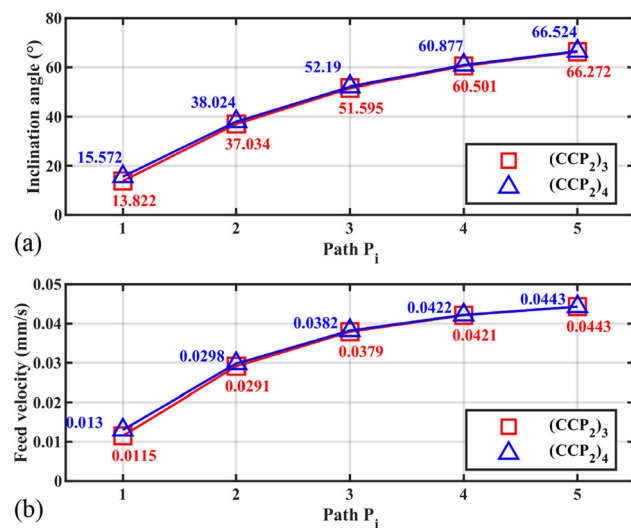
Fig. 26 Optimized process parameters: (a) inclination angle and (b) feed velocity

Fig. 27 (a) Five-axis CNC machine tool, (b) polishing process, and (c) unpolished workpiece
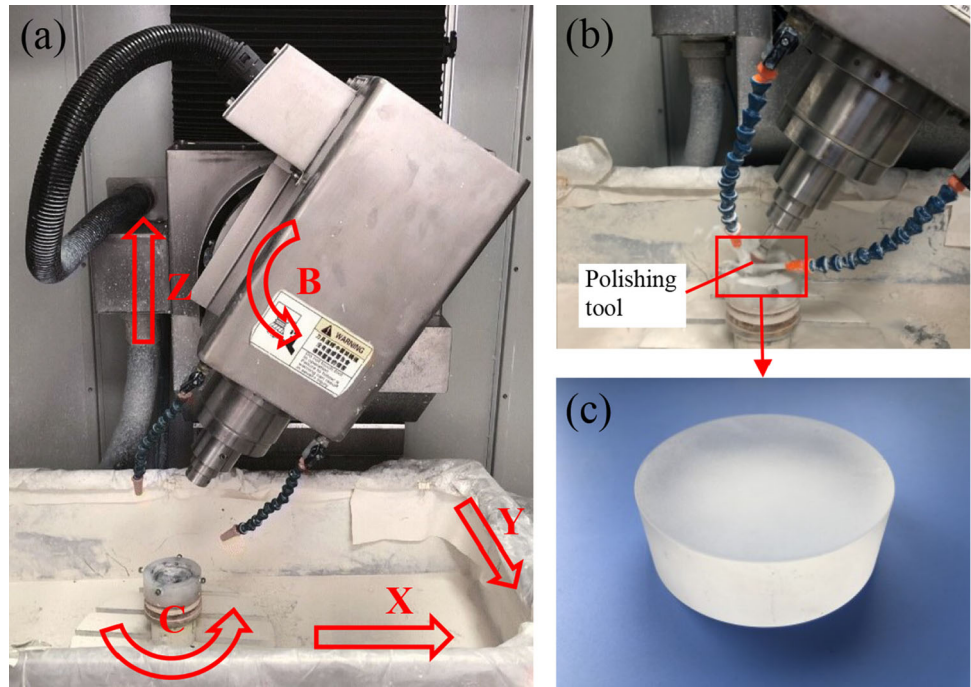
20mm, and the polishing paths and the process parameters were derived from the simulations in Section 4. The *X*-axis of CCP is selected as the measuring path *c*, and the surface profile and surface roughness of the workpiece were obtained by the profiler measuring along path *c*. The measured results of the surface profiles are shown in Fig. 32. The evaluation parameters of the surface profiles are calculated and shown in Table 9.

As can be seen from Fig. 32(a) and (b), the surface profile of the latter is smoother outside the central area. According to Table 9, the W_{opv} values for workpieces C1 and C2 are 11.881μm and 5.254μm, and the $W_{o\sigma}$ values for workpieces C1 and C2 are 2.280μm and 1.096μm, respectively. The reductions in the W_{opv} values and $W_{o\sigma}$ values show that the optimization methods of the spacing, inclination angle, and feed velocity proposed in Section 4.2 can effectively

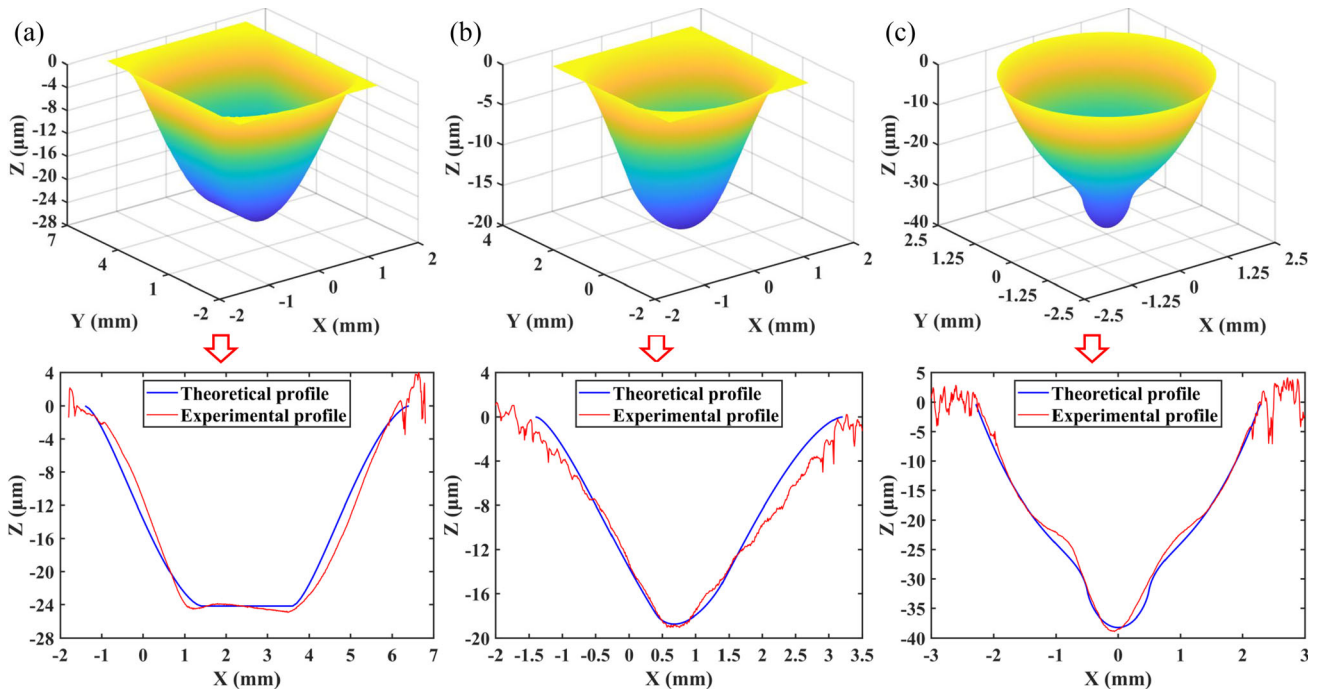**Fig. 28** (a) Taylor profiler, (b) measuring process, and (c) polished workpiece
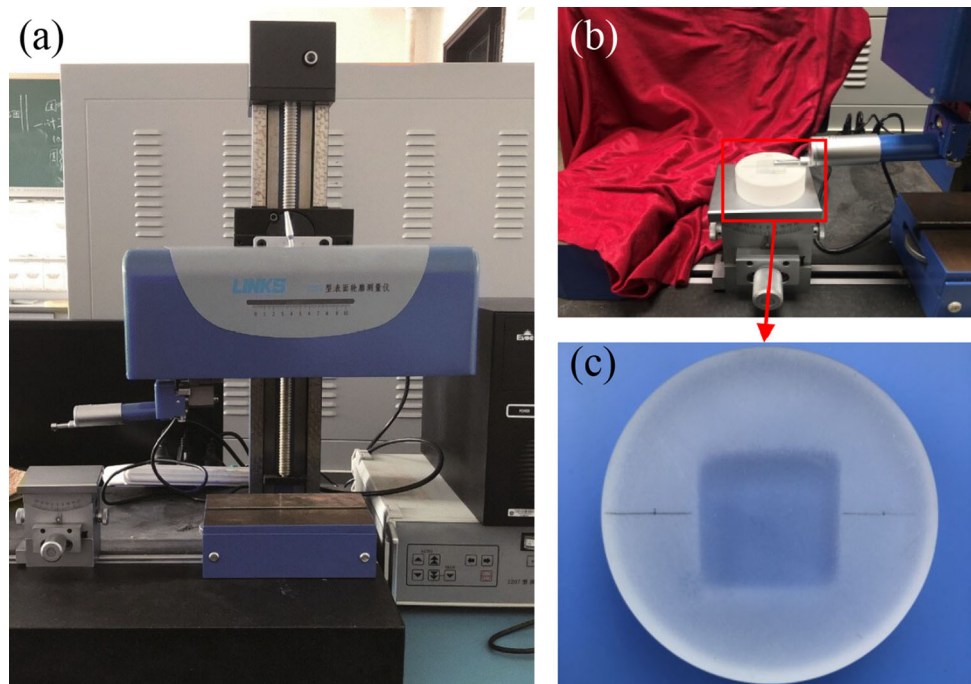
Fig. 29 Simulation and experimental results for special material removal model: (a) L=5mm; (b) L=2mm; (c) R=1.2mm
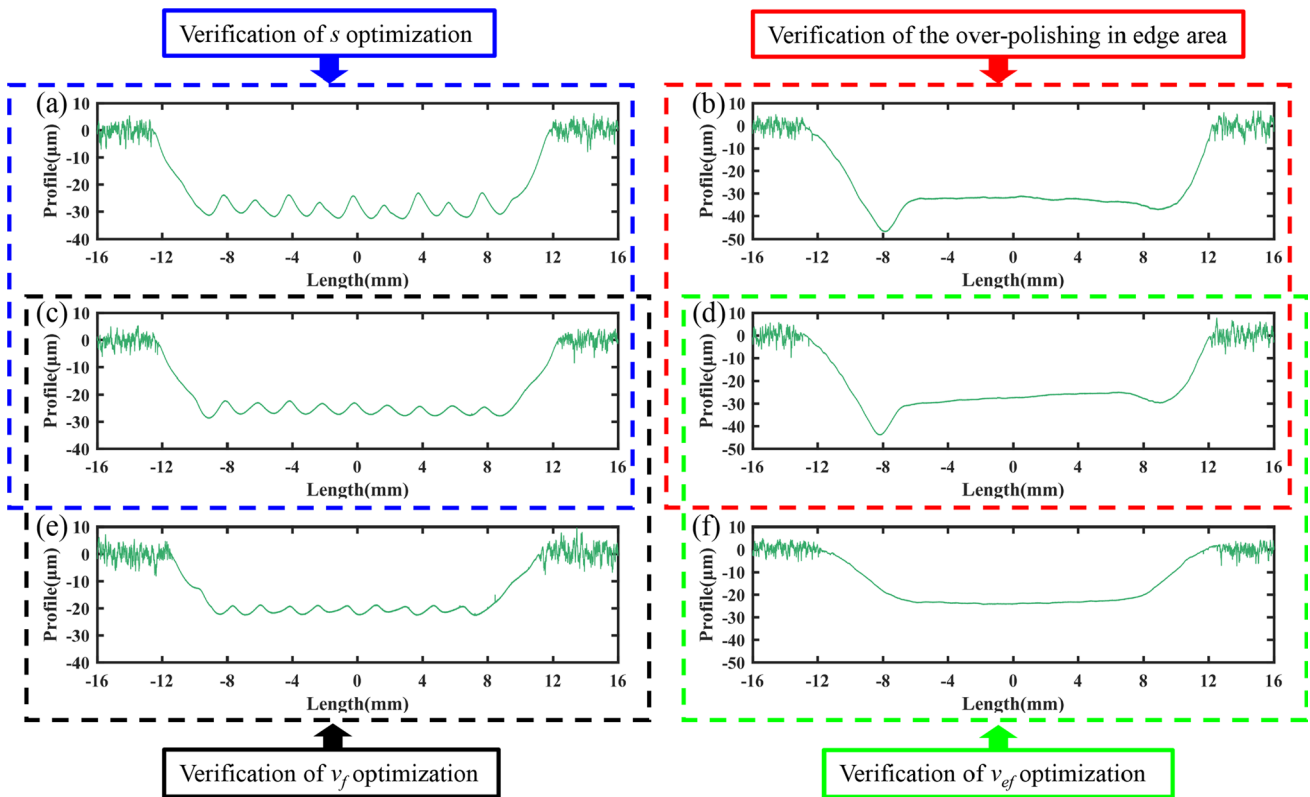

Fig. 30 Surface profile: (a) path a and (b) path b for workpiece A1, (c) path a and (d) path b for workpiece A2, and (e) path a and (f) path b for workpiece A3

Table 7 Experimental results

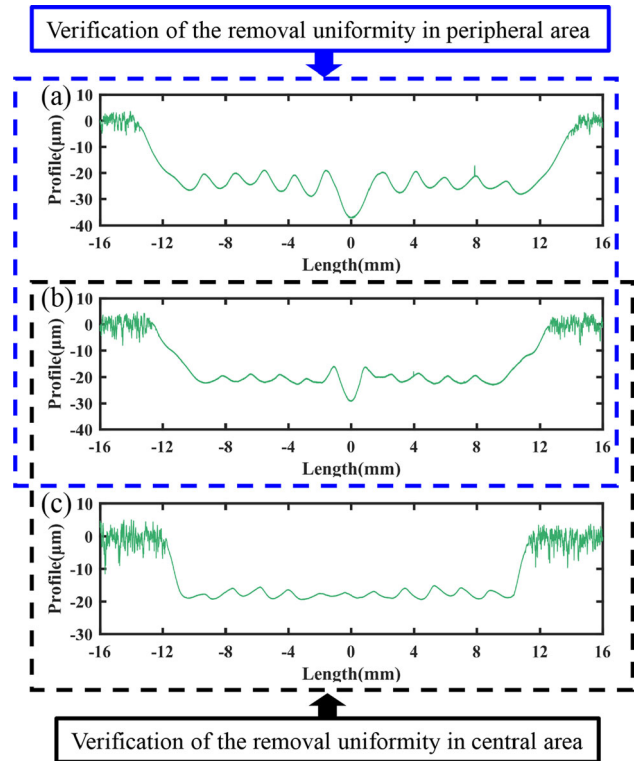| Workpiece	Path a (μm)				Path b			
	$H_{\max}$	W_{pv}	W_{σ}	Ra	$E_{\max}(\mu m)$	$E_{pv}(\mu m)$	r_{e1}	r_{e2}
A1	−32.765	9.767	2.562	0.0561	−46.729	23.731	1.426	2.430
A2	−28.692	6.500	1.517	0.0518	−43.873	21.681	1.529	3.336
A3	−22.688	4.006	1.031	0.0486	−23.580	4.898	1.039	1.223

improve the material removal uniformity. Moreover, the $H_{o\max}$ values for workpieces C1 and C2 are 29.122μm and 23.149μm respectively. The error between the $H_{o\max}$ value for workpiece C2 and the given removal thickness (20μm) is only 10%. It indicates that the optimization methods of posture angles and feed velocity proposed in Section 4.2 can control the material removal thickness. It can be seen from Fig. 32(a) and (c) that there is obvious over-polishing in the central area of CCP. Compared with Fig. 32(b) and (c), the surface profile in Fig. 32(c) is more gentle. The C_{pv} values for workpieces C2 and C3 are 13.360 and 2.5830, and the r_{c1} values for workpieces C2 and C3 are 1.263 and 0.9997, respectively. The reductions in the C_{pv} value and r_{e1} value show that the optimization methods of the radius R_1 of the central path, the spacing s, inclination angle δ_1,
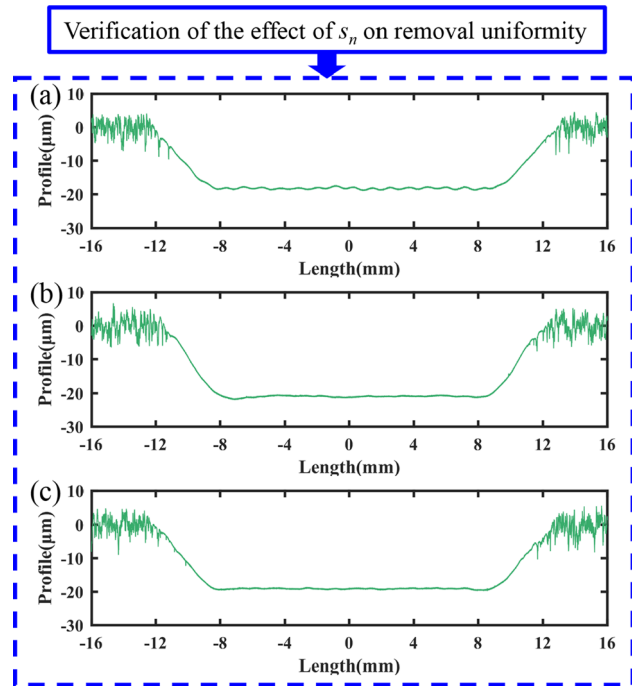
Fig. 31 Surface profile of path a for (a) workpiece B1, (b) workpiece B2, and (c) workpiece B3

Fig. 32 Surface profile of path c for (a) workpiece C1, (b) workpiece C2, and (c) workpiece C3

Table 8 Experimental results.(μm)

Workpiece	$H_{\max}$	W_{pv}	W_{σ}	Ra
B1	−18.956	1.594	0.252	0.0403
B2	−21.457	1.035	0.177	0.0382
B3	−19.521	0.838	0.126	0.0370

Table 9 Experimental results

Workpiece	Peripheral profile (μm)			Central profile				
	$H_{o\max}$	W_{opv}	$W_{o\sigma}$	$C_{\max}(\mu m)$	$C_{pv}(\mu m)$	r_{c1}	r_{c2}	$Ra(\mu m)$
C1	−29.122	11.881	2.280	−37.193	18.218	1.277	1.534	0.0619
C2	−23.149	5.254	1.096	−29.240	13.360	1.263	2.543	0.0549
C3	−19.441	4.343	1.076	−19.435	2.5830	0.9997	0.5948	0.0524

and feed velocity v_{a1} proposed in Section 4.3 can effectively eliminate the over-polishing in the central area.

6 Conclusion

How to ensure the uniformity of the global material removal by comprehensively optimizing the polishing path and material removal has been studied in this paper. Two common polishing paths are covered: the scanning path and the concentric circle path. The scanning path was divided into the inner area and edge area, and the concentric circle path was divided into the peripheral area and central area, respectively.

Firstly, material removals in the special cases of the straight path and circular path are modeled, and the material removal maps are calculated to analyze the global material removal caused by the scanning path and the concentric circle path.

For the scanning path, the spacing range is defined according to the number of superimposed removal profiles, and the optimal spacing value of each spacing range is determined by using the numerical method. Then, the feed velocity was optimized to control the material removal thickness in the inner area, eliminate the over-polishing in the edge area, and ensure the polishing efficiency.

For the concentric circle path, in the peripheral area, the influence of the path curvature on the removal profile is eliminated by optimizing the inclination angle and feed velocity, so that the spacing law of the scanning path can be applied to the concentric circle path. Furthermore, the over-polishing in the central area was improved by optimizing the radius of the central path, inclination angle, and feed velocity.

Simulation and experimental results show that the proposed method can significantly improve the material removal uniformity, control the removal thickness, and ensure the polishing efficiency.

Further work will be employed on the more complex surfaces and paths.

Declarations

Conflict of interest The authors declare no competing interests.

References

1. Ding YF, Min XP, Fu WW et al (2019) Research and application on force control of industrial robot polishing concave curved surfaces. Proc IMeche, Part B: Journal of Engineering Manufacture 233(6):1674–1686. https://doi.org/10.1177/0954405418802309
2. Zhai K, He Q, Li L et al (2017) Study on chemical mechanical polishing of silicon wafer with megasonic vibration assisted. Ultrasonics 80:9–14. https://doi.org/10.1016/j.ultras.2017.04.005
3. Liu P, Bae S, Hong S et al (2022) Investigation of thermal effects in copper chemical mechanical polishing. Precis Eng 73:195–202. https://doi.org/10.1016/j.precisioneng.2021.08.022
4. Choi YT, Wereley NM (2022) Controllable stress of magnetorheological fluid elastomeric encapsulations. IEEE Trans Magn 58(2):1–10. https://doi.org/10.1109/TMAG.2021.3085588
5. Guo Y, Yin S, Ohmori H et al (2022) A novel high efficiency magnetorheological polishing process excited by Halbach array magnetic field. Precis Eng 74:175–185. https://doi.org/10.1016/j.precisioneng.2021.11.011
6. Wang C, Zhang Z, Cheung CF et al (2022) Maskless fluid jet polishing of optical structured surfaces. Precis Eng 73:270–283. https://doi.org/10.1016/j.precisioneng.2021.09.010
7. Wan K, Wan S, Jiang C et al (2022) Sparse bi-step raster path for suppressing the mid-spatial-frequency error by fluid jet polishing. Opt Express 30(5):6603–6616. https://doi.org/10.1364/OE.453122
8. Wang Z, Wu L, Fang Y et al (2022) Application of flow field analysis in ion beam figuring for ultra-smooth machining of monocrystalline silicon mirror. Micromachines 13(2):318. https://doi.org/10.3390/mi13020318
9. Chernyshev A, Chkhalo N, Malyshev I et al (2021) Matrix based algorithm for ion-beam figuring of optical elements. Precis Eng 69:29–35. https://doi.org/10.1016/j.precisioneng.2021.01.006
10. Huang Z, Chen G, Liu H et al (2022) Research on robot bonnet polishing silicon carbide optical element machining method based on improved traveling salesman problem pseudo-random polishing path planning. Opt Eng 61(2):25102. https://doi.org/10.1117/1.OE.61.2.025102
11. Zhong B, Deng W, Chen X et al (2021) Frequency division combined machining method to improve polishing efficiency of continuous phase plate by bonnet polishing. Opt Express 29(2):1597–1612. https://doi.org/10.1364/OE.412678

12. Tian F, Lv C, Li Z et al (2016) Modeling and control of robotic automatic polishing for curved surfaces. CIRP J Manuf Sci Technol 14:55–64. https://doi.org/10.1016/j.cirpj.2016.05.010

13. Jin M, Wang L, Ye S et al (2020) A novel functionally graded lapping and polishing method for the improvement of material removal uniformity. J Manuf Process 50:102–110. https://doi.org/10.1016/j.jmapro.2019.12.039

14. Han Y, Zhang L, Guo M et al (2018) Tool paths generation strategy for polishing of freeform surface with physically uniform coverage. Int J Adv Manuf Technol 95(5-8):2125–2144. https://doi.org/10.1007/s00170-017-1281-2

15. Zhao Q, Zhang L, Han Y, Fan C (2019) Polishing path generation for physical uniform coverage of the aspheric surface based on the archimedes spiral in bonnet polishing. Proceedings of the Institution of Mechanical Engineers, Part B: Journal of Engineering Manufacture 233(12):2251–2263. https://doi.org/10.1177/0954405419838655

16. Zhang L, Han Y, Fan C et al (2017) Polishing path planning for physically uniform overlap of polishing ribbons on freeform surface. Int J Adv Manuf Technol 92(9-12):4525–4541. https://doi.org/10.1007/s00170-017-0466-z

17. Zhang L, Tam HY, Yuan CM et al (2002) An investigation of material removal in polishing with fixed abrasives. Proceedings of the Institution of Mechanical Engineers, Part B: Journal of Engineering Manufacture 216(1):103–112. https://doi.org/10.1243/0954405021519591

18. Tam HY, Zhang L, Hua M (2004) Material removal by fixed abrasives following curved paths. Proceedings of the Institution of Mechanical Engineers, Part B: Journal of Engineering Manufacture 218(7):713–720. https://doi.org/10.1177/095440540421800704

19. Fan C, Zhao J, Zhang L et al (2016) Local material removal model considering the tool posture in deterministic polishing.

20. Fan C, Zhao J, Zhang L et al (2014) Modeling and experimental study on the material removal in the velocity-dwell-mode polishing process. J Mech Eng 50(5):173–181. https://doi.org/10.3901/JME.2014.05.173

21. Tam HY, Hua M, Zhang L (2007) Aspheric surface finishing by fixed abrasives. Int J Adv Manuf Technol 34(5-6):483–490. https://doi.org/10.1007/s00170-006-0625-0

22. Fan C, Zhao J, Zhang L et al (2014) Predictive models of the local and the global polished profiles in deterministic polishing of free-form surfaces. Proceedings of the Institution of Mechanical Engineers, Part B: Journal of Engineering Manufacture 228(8):868–879. https://doi.org/10.1177/0954405413512813

23. Hy Tam, Cheng H (2010) An investigation of the effects of the tool path on the removal of material in polishing. J Mater Process Technol 210(5):807–818. https://doi.org/10.1016/j.jmatprotec.2010.01.012

24. Greenwood JA (1985) Formulas for moderately elliptical hertzian contacts. J Tribol 107(4):501–504. https://doi.org/10.1115/1.3261116

25. Greenwood JA (1997) Analysis of elliptical hertzian contacts. Tribol Int 30(3):235–237. https://doi.org/10.1016/S0301-679X(96)00051-5

Affiliations

Xingtian Qu[1] · Qinglong Liu[1] · Hongyi Wang[1] · Haizhong Liu[1] · Jiming Liu[1] · Huichao Sun[1]

Xingtian Qu
quxt@jlu.edu.cn

Qinglong Liu
1572992102@qq.com

Haizhong Liu
liuhaizhong@jlu.edu.cn

Jiming Liu
496527882@qq.com

Huichao Sun
sunhc@jlu.edu.cn

[1]   School of Mechanical and Aerospace Engineering, Jilin University, Renmin Street, Changchun, 130025, Jilin, People's Republic of China